Ceramics International 49 (2023) 34712–34725

Contents lists available at ScienceDirect

Ceramics International

journal homepage: www.elsevier.com/locate/ceramint

Se-doped Nb_2O_5–Al_2O_3 composite-ceramic nanoarrays via the anodizing of Al/Nb bilayer in selenic acid

Kirill Kamnev [b], Maria Bendova [a,b], Zdenek Pytlicek [b], Jan Prasek [a,b], Lukáš Kejík [b], Frank Güell [c], Eduard Llobet [d], Alexander Mozalev [a,b,*]

[a] Department of Microelectronics, Faculty of Electrical Engineering and Communication, Brno University of Technology, Technicka 10, 616 00, Brno, Czech Republic
[b] CEITEC – Central European Institute of Technology, Brno University of Technology, Purkynova 123, 61200, Brno, Czech Republic
[c] ENFOCAT-IN2UB, University of Barcelona, Marti i Franques 1, 08028, Barcelona, Catalonia, Spain
[d] MINOS, University Rovira i Virgili, Av. Paisos Catalans 26, 43007, Tarragona, Catalonia, Spain

ARTICLE INFO

Handling Editor: Dr P. Vincenzini

Keywords:
Al_2O_3–Nb_2O_5 nanocomposite
Anodizing
Selenic acid
Transition metal oxides
Porous anodic alumina
SERS

ABSTRACT

Novel arrays of Nb_2O_5-based ceramic nanostructures of various sizes (9–210 nm) and morphologies (dots, goblets, rods) aligned on substrates are fabricated via the anodizing of a thin Nb film through the initially formed porous anodic alumina (PAA) film in 1.5 M selenic acid (H_2SeO_4) – a new aqueous electrolyte generating extraordinarily thinner PAA pores than any other solutions. Accordingly, the nanostructures formed in the selenic acid are 1.3-fold thinner and better self-ordered than their counterparts formed from the same Al/Nb precursor bilayer in a reference oxalic-acid electrolyte. The nanostructures have a dual (core/shell) composition: the inner material (the core) is stoichiometric Nb_2O_5, whereas the outer layer (the shell) is a few nm-thick substoichiometric NbO_x mixed with Al_2O_3. The composite-ceramic nanoarrays grow doped with selenium species such as selenate (SeO_4^{2-}) and selenide (Se^{2-}) anions originating from the electrolyte and migrating inward under the high electric field. The incorporated Se species do not contribute to photoluminescence emission nor hinder the Raman signal from the nanoarrays, which makes them highly promising as Nb_2O_5-based SERS biosensing substrates. The planar PAA-inbuilt Se-doped Nb_2O_5–Al_2O_3 nanostructured ceramic film performs like a high-*k* low-loss low-leakage-current dielectric promising for on-chip integration. More potential applications of the Se-doped ceramic nanoarrays developed here include biomedical antibacterial coatings, advanced superhydrophobic surfaces, gas-sensing, and catalytic layers.

1. Introduction

Niobium pentoxide (Nb_2O_5) and its compounds with other transition-metal oxides are attractive ceramic materials for catalysis, biomedicine, and surface protection applications [1–3]. Niobium pentoxide is also actively utilized as a building block for photovoltaic, sensing, energy storage, electrochromic, electronic, and optical devices [4–9]. For many modern applications, nanostructuring of Nb_2O_5-based ceramics is required to enhance the material's characteristics, increase the surface-to-volume ratio, and possibly introduce novel properties. Commonly used nanostructuring techniques are the sol-gel, ion-beam sputtering, chemical vapor deposition, and atomic layer deposition [7,10,11]. A method based on electrochemical anodizing of a thin layer of aluminum (Al) superimposed on a layer of niobium (Nb) has recently been developed to synthesize self-ordered arrays of Nb_2O_5 nanostructures with controllable dimensions [12]. First, the Al layer is anodized to form a porous anodic alumina (PAA) film. The underlying Nb is then anodized through the superimposed PAA layer (the so-called PAA-assisted *anodizing*), forming Nb_2O_5 nuclei within and beneath the barrier layer of the PAA film. Subsequent PAA-assisted high-voltage *re-anodizing* transforms the Nb_2O_5 nuclei into longer oxide nanostructures such as columns or rods via the growth of niobium oxide inside the PAA nanopores [13]. Selective dissolution of the PAA overlayer yields arrays of upright-standing and spatially separated Nb_2O_5 semiconductor nanostructures advantageous for gas-sensing and surface-finishing applications [2,4,14].

Precise control over the surface morphology and chemical composition of Nb_2O_5 nanostructures is crucial for advancing existing and

* Corresponding author. Department of Microelectronics, Faculty of Electrical Engineering and Communication, Brno University of Technology, Technicka 10, 616 00, Brno, Czech Republic.
E-mail address: mozalev@vut.cz (A. Mozalev).

https://doi.org/10.1016/j.ceramint.2023.08.134
Received 25 April 2023; Received in revised form 30 July 2023; Accepted 11 August 2023
Available online 12 August 2023

developing new applications of niobium-oxide-based nanomaterials [15]. The fundamental and functional properties of the PAA-assisted Nb_2O_5 ceramic nanoarrays can be controlled by simply adjusting the electrical and electrolytic formation conditions [12,14,16]. The nature of the anodizing electrolyte and the formation voltage decide the areal density and diameters of the PAA nanopores. In turn, these PAA properties govern the population density and diameters of the PAA-assisted niobium-oxide nanostructures. The relation has been experimentally proved in several anodizing electrolytes such as sulphuric, oxalic, phosphoric, and citric acids [2,4,12,13].

An aqueous solution of **selenic acid** (H_2SeO_4) has recently been explored as a novel PAA-forming electrolyte generating substantially thinner pores than any other acid electrolyte at the same formation voltages [17]. Consequently, the porosity of the PAA films grown in selenic acid (2–3%) decreases by 3-fold compared with other anodizing electrolytes (6–10%). The uniquely low porosity of PAA formed in selenic acid appeared highly advantageous for fabricating photonic crystals and synthesizing metamaterials [18,19].

Suppose niobium can be anodized through the PAA films formed in selenic acid. In that case, the unique porous-cellular structure of the PAA films might be 'transferred' to the anodic niobium oxide and promote the growth of extremely thin but long-distanced niobium-oxide nanocolumns or rods. Such nano-morphology could be in demand for modulating Nb_2O_5 surface-plasmon resonance (SPR) because the effect largely depends on the relation between the width and spatial separation of the nanostructures [19]. The possibility to tune the SPR of the Nb_2O_5 nanoarrays makes them particularly promising in the emerging niobium-oxide application as a substrate for surface-enhanced Raman spectroscopy (SERS) [20]. Moreover, due to the lowered contact area between the liquid and the solid, the extremely thin and long-distanced Nb_2O_5 nanostructures are preferred for engineering superhydrophobic ceramic coatings [2,21]. Further, the extraordinarily thin PAA nanopores formed in selenic acid may effectively suppress the field crystallization of growing niobium oxide by limiting the space available for crystal formation. Such arrays of amorphous Nb_2O_5 nanostructures can hardly be synthesized by other methods and are in demand for various electric/dielectric applications due to isotropy of properties, lack of interfacial defects, and absence of leakage paths through the crystalline grain boundaries, as reported elsewhere [22].

It is known that electrolyte-derived species readily incorporate into both PAA and PAA-assisted niobia nanostructures during anodization and affect the oxides' chemical composition and functional properties [13]. For example, the incorporation of phosphorous (P), carbon (C), sulfur (S), chromium (Cr), or boron (B) from acid electrolytes may result in oxide coloration, reduced optical transparency, and wide-spectrum fluorescence [23]. On the other hand, the PAA formed in selenic acid is reportedly highly transparent and produces no unwanted fluorescence [24–26]. Therefore, it is anticipated that PAA-assisted niobium anodizing in selenic acid may result in nanostructured Nb_2O_5 ceramics with similarly unhindered optical properties. The lack of optical-signal contamination is especially desired for the emerging application of Nb_2O_5 in SERS due to the fundamental intersection of Raman scattering with fluorescence [27].

Furthermore, Se species are known to have potent antibacterial and anti-oncogenic properties. Incorporating Se species into PAA-assisted Nb_2O_5 ceramic nanostructures via anodizing in selenic acid can boost the oxide's biomedical characteristics and facilitate its application as implant coating [28,29]. High anti-oxidative properties of adsorbed or incorporated Se species can also enhance the activity of the nanostructured Nb_2O_5 and Nb_2O_5/Al_2O_3 catalysts [30–32]. Lastly, Se might bond with Nb to form a $NbSe_2$ compound with the nanoscale periodic morphology desired for emerging electronic applications [33].

In the present work, for the first time, Nb_2O_5-based ceramic nanoarrays were fabricated via the PAA-assisted anodizing and higher-voltage re-anodizing of a thin Nb film in selenic acid. The influence of the formation conditions on the morphology, chemical composition, mixing with Al_2O_3, selenium incorporation, and several practically important functional properties of the Se-doped niobium-oxide-based nanoceramics were studied by high-resolution scanning electron microscopy (SEM), X-ray photoelectron spectroscopy (XPS), Raman spectroscopy, photoluminescence (PL) spectroscopy, and electrical/dielectric measurements. To prove the morphological advantages of the PAA-assisted ceramic nanoarrays formed in the selenic-acid electrolyte, they were directly compared with those synthesized in an oxalic-acid electrolyte at the same formation voltages. A mechanism for the PAA-assisted selenic-acid niobium anodizing was proposed and experimentally justified. Potential applications of the Se-doped Nb_2O_5-based ceramic nanoarrays as advanced SERS biosensing substrates, superhydrophobic surfaces, biomedical coatings, catalytic, gas-sensing, and high-*k* planar nanocomposite dielectric layers for on-chip integration were experimentally and theoretically appraised.

2. Experimental section

2.1. Sample preparation

A standard 4″ Si wafer covered by a 380-nm SiO_2 layer was used as the starting substrate. A 140-nm niobium layer followed by a 1000-nm aluminum layer was deposited on the substrate by the magnetron sputtering of Nb (99.95%) and Al (99.999%) targets to make a precursor Al/Nb bilayer. The wafer with the deposited bilayer was cut into ca. 1 cm × 1 cm pieces. The individual samples were anodized in 1.5 M H_2SeO_4 aqueous solution at room temperature (21 °C). A custom-made polytetrafluoroethylene two-electrode cell securing a 0.8 cm^2 circular working area was used as the anodizing bath [34]. A 6 mm in diameter glassy carbon rod, distanced by 3 mm from the sample surface, was employed as the cathode. The PAA films were formed at a constant current density of either 5.0 or 0.5 mA cm^{-2}, resulting in a steady-state voltage of 42 or 12 V, respectively. Selected samples were re-anodized using a high-speed (10 V s^{-1}) potentiodynamic polarization up to 120 or 80 V, followed by a potentiostatic polarization to ensure uniform oxide growth across the sample surface. The PAA overlayer was dissolved from selected samples in an aqueous solution of 0.2 M Cr_2O_3 and 0.45 M H_3PO_4 at 65 °C for 1 h [35]. Hereafter, samples with the dissolved PAA layer are named the 'PAA-free' samples. After the anodizing/re-anodizing and PAA dissolution, the samples were thoroughly rinsed in Milli-Q® ultrapure water, dried in a nitrogen stream, and heated in an oven at 393 K for 1 h to desorb the water molecules from the oxide surface.

2.2. Sample analysis

The surfaces and cross-fractures of PAA-free samples were examined in an FEI Verios 460L High-Resolution **SEM** operated at 15 kV accelerating voltage and 0.8 nA probe current. The chemical composition of the film surfaces was analyzed by **XPS** in a Kratos Axis Ultra DLD spectrometer using a monochromatic Al Kα source. The X-ray emission power was 150 W with a 15 kV accelerating voltage focused to a 300 μm × 700 μm spot. Typical operating pressures were better than 10^{-9} Torr. The emitted electrons were detected by a hemispherical analyzer at fixed pass energies of 160 eV for the survey and 20 eV for the high-resolution spectra. The Kratos charge neutralizer system was used for all specimens. The depth profiling was performed using an argon-ion beam of 5 kV provided by a standard ion gun with a sample current of 750 nA scanned over a surface window of 2 mm × 2 mm for 90 and 270 s, resulting in slight surface etching. The sputtering-beam incidence angle was 45° relative to the substrate. Spectra were analyzed using CasaXPS (ver. 2.3.17) software. GL(30) profiles, defined in CasaXPS, were used for all components besides the metallic core lines of Nb 3d, for which asymmetric profiles in the form of LA(1.2,5,12) were used. A standard Shirley background was used in all fitted spectra. Spectra from all samples were charge corrected to give the adventitious C 1s spectral

component (C–C, C–H) binding energy of 284.8 eV. The deconvolution of C 1s spectra was performed as described in previous works [13]. Quantitative analysis was performed using the narrow spectra and relative sensitivity factors from CasaXPS suitable for Kratos Axis Ultra, referenced to F 1s.

Selected PAA-free samples were analyzed by **PL spectroscopy** using a chopped Kimmon IK Series He–Cd laser (325 nm and 40 mW). The fluorescence was dispersed with an Oriel Corner Stone 1/8 74000 monochromator, detected using a Hamamatsu H8259-02 with a socket assembly E717-500 photomultiplier, and amplified through a Stanford Research Systems SR830 DSP. Selected PAA-free samples were analyzed by **Raman spectroscopy** using the WITec confocal Raman imaging system alpha300 R. The samples were illuminated by a 532 nm laser with power reduced to 1 mW and focused by 100× objective (NA 0.9).

2.3. Electrical characterization

Electrical measurements were conducted using test metal-insulator-metal (MIM) devices. A 100 nm-thick Nb layer followed by a 65 nm-thick Al layer (Al/Nb bilayer) were deposited by the magnetron sputtering onto a SiO_2-coated Si wafer. A piece of 1.5 cm × 1.5 cm cut from the wafer was anodized at 0.5 mA cm^{-2} and then re-anodized to 70 V at a rate of 10 V s^{-1} using the methodology and anodizing setup described in section 2.1. Such anodizing was expected to generate a planar film where the PAA-assisted Nb_2O_5 nanostructures grow up to the PAA-surface level. For making the top electrodes, a layer of ~100 nm-thick platinum (Pt) was sputter-deposited through an array of 10 μm × 10 μm square openings in a thin ceramic plate used as the shadow mask. The unoxidized Nb layer that remained under the anodic film after the re-anodizing served as the bottom electrode. The assembled MIM microdevices were mounted to Cascade Microtech MPS 150 Probe Station connected to an Agilent Technologies Precision LCR Meter E4980A and a Keithley 4200A-SCS Parameter Analyzer. Unless otherwise specified, the top Pt contacts were used as a cathode in electrical tests.

3. Results and discussion

3.1. Anodizing behavior

Typical voltage- and current-time responses during the 5.0 and 0.5 mA cm^{-2} anodizing of the sputter-deposited Al/Nb bilayer in 1.5 M H_2SeO_4 aqueous solution, followed without interruption by 120 and 80 V high-speed re-anodizing in the same electrolyte, are presented in Fig. 1. Both responses generally exhibit similar behavior and can be divided into three distinct stages. 1st stage: The voltage-time curves are typical for the porous anodizing of aluminum in acid electrolytes, including the PAA formation on aluminum foils in selenic-acid electrolytes of comparable concentration reported elsewhere [24,36]. Systematic growth of PAA film is associated with the periods when the voltage attains the steady-state values, U_{st}, of ~42 V (hereafter the 'high-voltage' sample) or ~12 V (the 'low-voltage' sample). Once the anodizing front reaches the niobium underlayer, the voltage begins to increase, and the process is automatically switched into the potentiostatic mode at 45 or 13 V, respectively. 2nd stage: The behavior is determined by the 'smart' PAA-assisted anodizing of the niobium underlayer: arrays of niobium-oxide nanostructures nucleate and grow downward into the Nb metal and upward into the PAA barrier layer [13]. The applied voltage and the length of the current decay impact the oxide growth. 3rd stage: The high-speed potentiodynamic re-anodizing up to 120 V (Fig. 1a) or 80 V (Fig. 1b) is followed without interruption by a short potentiostatic polarization with a current decay. The niobium oxide is expected to grow further and partially fill the PAA pores at this stage [13]. This process will likely compete with expanding the nanostructures' bases, which can merge in a continuous bottom oxide layer. The merging of the bases depends on a combination of factors like the nanostructures' dimensions, the ratio of ionic resistances

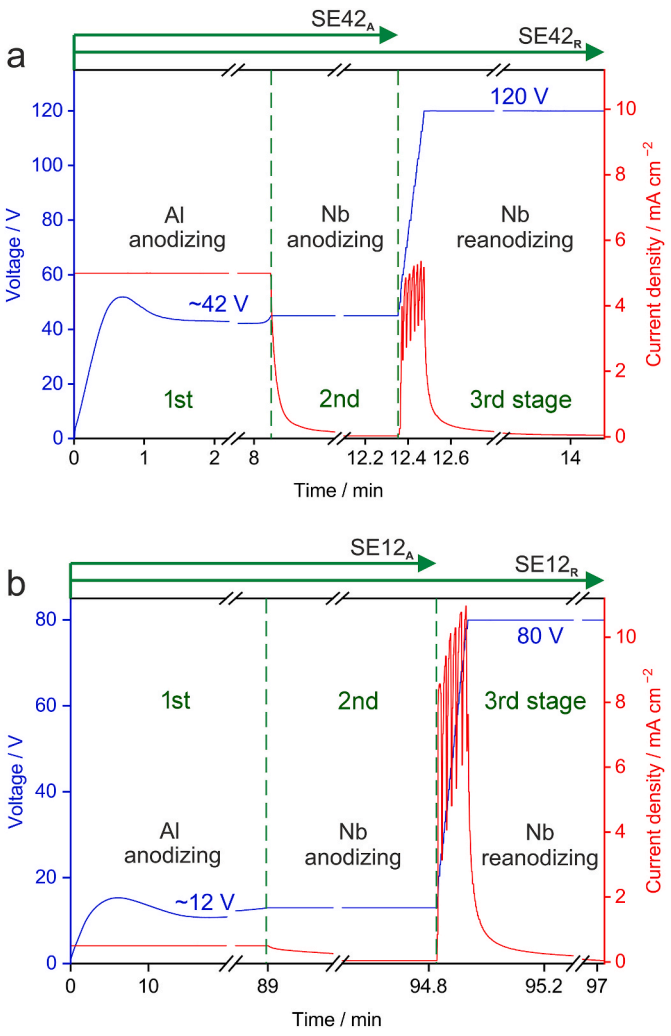

Fig. 1. Voltage- and current-time responses during the anodic processing of Al (1000 nm)/Nb (140 nm) bilayer in 1.5 M H_2SeO_4 aqueous electrolyte at 21 °C for forming Nb_2O_5 nanoarrays: 1st stage – the galvanostatic aluminum anodizing for forming porous anodic alumina (PAA) at (a) 5 mA cm^{-2} (steady-state voltage U_{st} = 42 V) and (b) 0.5 mA cm^{-2} (U_{st} = 12 V); 2nd stage – the potentiostatic PAA-assisted niobium anodizing at (a) 45 V and (b) 13 V; 3rd stage – the potentiodynamic PAA-assisted niobium re-anodizing with a rate of 10 V s^{-1} to (a) 120 V and (b) 80 V followed by potentiostatic polarization at the same voltages. The samples are named relating to the selenic (SE) acid, U_{st}-values (12 or 42 V), and the formation stages (A: anodizing till the end of 2nd stage, R: re-anodizing: till the end of 3rd stage), as specified above the plots.

between alumina and niobia, ionic transport numbers, anion incorporation, oxide crystallization behavior, etc.

In the following text, the samples will be distinguished by their U_{st} during the 1st stage (Fig. 1): The high- and low-voltage samples prepared by the selenic-acid *anodizing* to the end of the 2nd stage will be named **$SE42_A$** and **$SE12_A$**, respectively. The high- and low-voltage samples prepared by the selenic-acid anodizing followed by re-anodizing to the end of the 3rd stage will be named **$SE42_R$** and **$SE12_R$**, respectively.

3.2. Film morphology

Fig. 2 shows SEM images of the PAA-free $SE42_A$ and $SE42_R$ samples. The $SE42_A$ surface (Fig. 2a) reveals an array of upright-standing, spatially separated nanosized protrusions, presumably of niobium oxide. The protrusions are surrounded by an unoxidized metal, likely Al. From Fig. 2c, the shape of the protrusions resembles a 'goblet'. The

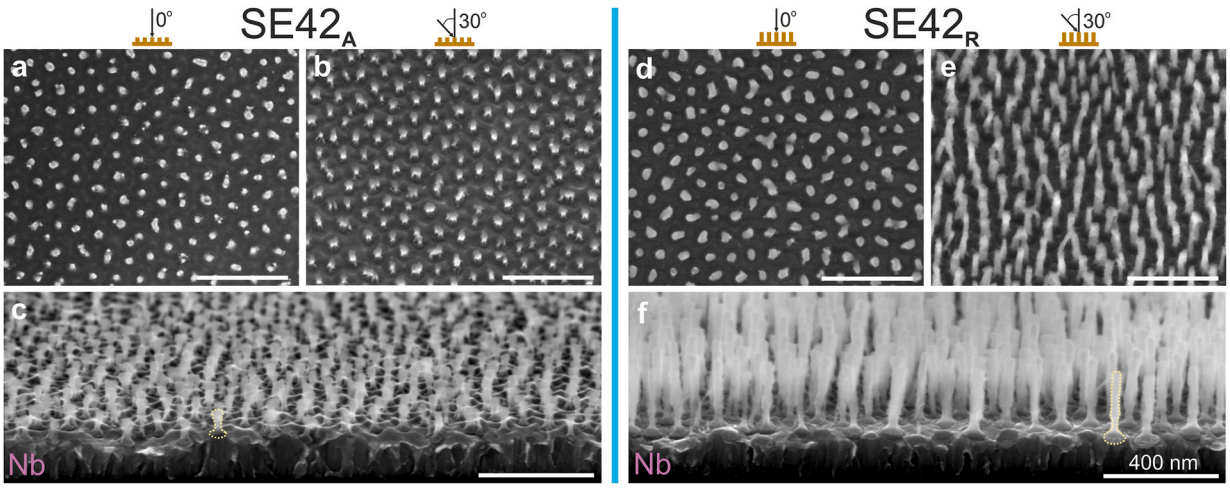

Fig. 2. SEM (a and d) vertical surface views, (b and e) 30°-tilted surface views, and (c and f) 3D cross-fracture views of niobium-oxide nanoarrays derived from an Al/Nb bilayer anodized and re-anodized in 1.5 M selenic acid as defined and named in Fig. 1a. The PAA layers were selectively dissolved away before SEM observation. All undefined scale bars are 400 nm.

nanogoblets' apexes gradually transit to relatively thinner middle parts, often composed of several distinguished nanoroots that expand to form broader bases. The bases are separated from each other by unoxidized niobium metal.

Fig. 2d–f depicts the $SE42_R$ film morphology. From the surface view, the horizontal projections of the protrusions thicken with re-anodizing. The protrusions become substantially longer and acquire the shape of rods, each having a single root that is relatively thinner than the rod's body. Although more expanded, the bases of the nanorods are still separated by the unoxidized Nb metal. The SEM analysis cannot reliably confirm the presence of unoxidized aluminum.

SEM images of the $SE12_A$ and $SE12_R$ samples are shown in Fig. 3. The upright-standing sub-10 nm oxide protrusions populate the $SE12_A$ surface (Fig. 3a). They have significantly smaller diameters and higher population density than the $SE42_A$ nanogoblets. From Fig. 3c, the nanoprotrusions are dot-shaped. The individual nanodots seem separated by the unoxidized Nb metal. The insufficient SEM resolution makes it impossible to judge the presence of an unoxidized aluminum. The surface view in Fig. 3d shows that the oxide protrusions expand with re-anodizing. The apexes of the protrusions tend to conglomerate in small groups, likely due to van der Waals forces. From Fig. 3f, the re-anodizing noticeably elongates the $SE12_A$ oxide nanodots, resulting in an array of rod-like nanostructures. A substantial difference between $SE12_R$ and the other films is that the bases of the nanorods merge in a continuous 30 nm-thick oxide layer that buffers the rods from the unoxidized Nb metal. Apparently, there is no unoxidized Al at the film surface.

3.3. Comparison between selenic- and oxalic-acid anodizing

The PAA-assisted niobium-oxide nanostructures grow inside and beneath the pores during the anodizing and re-anodizing [13]. Therefore, the PAA porous-cellular structure decides the diameters and surface distribution of the niobium-oxide nanoprotrusions. The pore center-to-center distance, D_{int}, is known to depend on U_{st} (the 1st stages in Fig. 1a and b) through a constant $k = 2.5$ nm V^{-1} per linear relation $D_{int} = kU_{st}$ [37]. Consequently, the center-to-center distance between the niobium-oxide nanostructures, D_{cent}, should be dependent on D_{int} and U_{st}:

$$D_{cent} = D_{int} = kU_{st} \quad (1)$$

Since the PAA layer can be grown in the selenic- and oxalic-acid electrolytes at the same U_{st}, one may expect that the subsequently

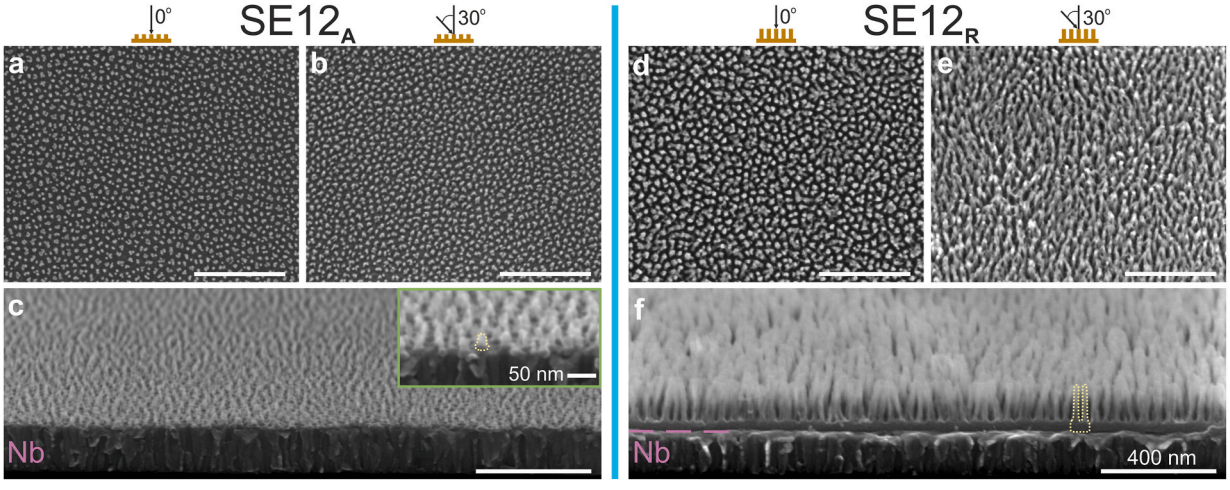

Fig. 3. SEM (a and d) vertical surface views, (b and e) 30°-tilted surface views, and (c and f) 3D cross-fracture views of niobium-oxide nanoarrays derived from an Al/Nb bilayer anodized and re-anodized in 1.5 M selenic acid as defined and named in Fig. 1b. The PAA layers were selectively dissolved away before SEM observation. All undefined scale bars are 400 nm.

formed niobium-oxide nanostructures would have similar D_{cent}. On the other hand, the PAA-assisted selenic-acid anodizing is expected to lead to niobium-oxide nanostructures with noticeably smaller diameters, d_n, due to the smaller PAA pore diameters, d_p, compared with the PAA-assisted oxalic-acid anodizing. Although the nanostructures formed in the selenic acid may have a D_{cent} similar to those formed in the oxalic acid, they should possess a smaller d_n and, therefore, acquire an advanced surface structuring, which is not attainable in other electrolytes. Since sensing, SPR, surface protection, self-cleaning, and biomedical properties of the oxide depend on the nanostructures' geometry and their mutual arrangement, the new morphology of the PAA-assisted nanostructures formed in the selenic acid could be especially relevant for the emerging applications of Nb_2O_5 ceramics.

For direct comparison, samples were prepared in 0.6 M oxalic acid ($H_2C_2O_4$) via the anodizing/re-anodizing of the same Al/Nb precursor bilayer. To this end, the current densities for PAA formation were adjusted to allow U_{st} of 42 and 12 V – the same as for the selenic-acid anodizing. Similarly, the niobium underlayer was re-anodized in the oxalic acid via the potentiodynamic polarization at 10 V s^{-1} up to 120 or 80 V. The samples formed by the PAA-assisted oxalic-acid anodizing will be named $OX42_A$, $OX42_R$, $OX12_A$, and $OX12_R$, corresponding to their counterparts SE42A, $SE42_R$, $SE12_A$, and $SE12_R$ formed in the selenic acid.

Fig. S1–S4 shows a side-by-side comparison of the nanostructures formed in the two electrolytes. The SEM data were quantified using ImageJ software to assess the mean values of nanostructures' dimensions summarized in Table 1. The D_{cent} and d_n values were plotted and best fitted with a normal distribution (Figs. S5–S7). D_{cent} and population density, ρ_N, were evaluated only for the anodized samples because the re-anodizing elongates the niobium-oxide nuclei without affecting their mutual arrangement. Moreover, the thin $SE12_R$ and $OX12_R$ nanorods tend to agglomerate, complicating image evaluation. From Figs. S1, S3, S6, and S7, one may see that the nanodots and nanogoblets formed in the selenic acid are substantially better self-ordered than the corresponding nanostructures formed in the reference oxalic-acid electrolyte.

Despite the same U_{st}, the nanostructures formed in the selenic acid reveal about 10% smaller D_{cent} and correspondingly slightly larger ρ_N than the nanostructures formed in the oxalic acid. Similarly, a ~10% smaller D_{int} was reported by Kikuchi et al. for the PAA formed on aluminum foil in selenic-acid electrolytes of comparable concentrations [24].

No electrolyte-dependent differences were revealed for the length of the niobium-oxide nanoprotrusions, h (Table 1, Figs. S1–S4). The $SE12_A$ and $OX12_A$ nanodots having $h = 20$ nm are both elongated to the 125 nm-tall $SE12_R$ and $OX12_R$ nanorods by the 80 V re-anodizing. Similarly, the $SE42_A$ and $OX42_A$ nanogoblets having $h = 75$ nm grow further to become the 210 nm-tall $SE42_R$ and $OX42_R$ nanorods after the 120 V re-anodizing. The $SE12_R$ and $OX12_R$ nanorods are anchored to a continuous ~30 nm-thick bottom-oxide layer. In contrast, the $SE42_A$ and $OX42_A$ nanogoblets and the $SE42_R$ and $OX42_R$ nanorods reside on convex-shaped bases separated by the unoxidized Nb. The bases of the $OX42_R$ nanorods seem slightly larger than those of the $SE42_R$ nanorods.

Further morphological differences between the nanostructures formed in the selenic and oxalic acids are associated with their diameters d_n. Based on the SEM analysis, we note the following major trends: (1) d_n decreases by ~30% for the nanostructures formed in the selenic acid. The effect is apparently due to the relatively thinner PAA nanopores grown by selenic-acid anodizing. (2) d_n increases by ~35% due to the re-anodizing in both acids. This effect could be explained by the partial growth of the rods within the inner part of the PAA cell walls, which is enabled by the upward migration of Nb cations through the PAA cell walls [13]. The cell walls may provide an effective pathway for ion transport due to defects such as vacancies and electrolyte-derived impurities, as described elsewhere [13,38].

The dimensions of PAA films formed in both acids were assumed based on the measured D_{cent} and theoretical considerations summarized in Fig. S8. One may see that d_n systematically exceeds d_p in all the samples (Table 1, Fig. S9). The degree of niobium-oxide expansion into the PAA cell walls was assessed by comparing the porosity [37] of the PAA films, $P = 0.907 d_p^2/D_{int}^2$, with the niobium-oxide nanostructures' projected area, $A = 0.907 d_n^2/D_{cent}^2$. It was revealed that A consistently exceeds P. In addition, A increases approximately by 2-fold after the re-anodizing. Another important revelation is that the A-value of the low-voltage samples (12/80 V) is about two times higher compared with the high-voltage samples (42/120 V) regardless of the electrolyte. Such a difference in A-values may arise because the anodic-oxide growth within the thinner pores of the low-voltage PAA is more obstructed. In such thin pores, the migration of Nb cations becomes more prevalent within the cell walls under the high electric field. Additionally, the effect may be due to the different ratios of the re-anodizing and steady-state voltage: for the low-voltage samples (80/12 V), the voltage ratio is 6.7, while for the high-voltage samples (120/42 V), the ratio is only 2.9. It is assumed that the higher the ratio, the more intensive the cation migration within the PAA cell walls.

The most practically important finding is that the nanostructures formed in the selenic acid exhibit, on average, a 1.5-fold lower A than their counterparts formed in the oxalic acid. Since the nanostructures' projection area (A) is the criterion to access the fundamental, structural, and functional benefits of the PAA-assisted oxide nanorods, the selenic-acid anodizing is experimentally justified. The high-voltage samples look most advantageous for niobium-oxide nanoarray applications, such as SPR and self-cleaning surfaces, where the lowest possible A is desired. The structural, compositional, and application-related benefits of the niobium-oxide nanostructured ceramics formed by the PAA-assisted selenic-acid anodizing are further discussed in section 3.6.

3.4. Nanostructures' chemical composition

The examination of chemical composition and bonding states in the

Table 1
Comparison of the PAA-assisted niobium-oxide nanoarrays synthesized in 1.5 M selenic acid (H_2SeO_4) and 0.6 M oxalic acid ($C_2H_2O_4$) electrolytes under the same anodizing/re-anodizing voltages.

	1.5 M H_2SeO_4 (selenic acid)				0.6 M $C_2H_2O_4$ (oxalic acid – reference)			
	$SE42_A$	$SE42_R$	$SE12_A$	$SE12_R$	$OX42_A$	$OX42_R$	$OX12_A$	$OX12_R$
Current density /mA cm^{-2}	5.0		0.5		12.2		1.3	
Steady-state voltage (U_{st}) /V	42		12		42		12	
Re-anodizing voltage /V	–	120	–	80	–	120	–	80
Center-to-center (D_{cent}) /nm	96 ± 9		27 ± 6		104 ± 14		30 ± 7	
Population density (ρ_N) /cm^{-2}	$1.2 \cdot 10^{10}$		$1.6 \cdot 10^{11}$		$1.1 \cdot 10^{10}$		$1.3 \cdot 10^{11}$	
Length (h) /nm	75	210	20	125	75	210	20	125
Nanostructure diameter (d_n) /nm	24 ± 4	35 ± 6	9 ± 2	13 ± 3	32 ± 6	45 ± 7	12 ± 3	17 ± 4
PAA pore diameter (d_p) /nm	16.2		4.2		24.2		7.2	
Nanostructure projected area (A) /%	5.7	12.0	10.0	21.0	8.6	17.0	14.5	29.1
PAA porosity (P) /%	2.5		2.2		4.9		5.2	

niobium-oxide nanoarrays formed by the PAA-assisted selenic-acid anodizing was performed by XPS (Fig. 4), mainly for the PAA-free samples. In addition, a $SE42_R$ sample with partially dissolved PAA, as sketched in the inset of Fig. 4m, was analyzed. In such a sample, about ~40 nm of the upper parts of the rods protrude outwards from the PAA surface level. This sample with the *partially-dissolved* PAA is hereafter named $SE42_{Rpd}$.

For comparison, a compact niobium-oxide film was prepared by potentiodynamic anodization of an Nb layer in 1.5 M selenic acid at a rate of 0.1 V s^{-1} up to 10 V. The initial Nb layer was obtained by dissolving the Al layer from the Al/Nb precursor bilayer in 1 wt% NaOH solution. XP spectra were recorded on the as-prepared (not sputter-cleaned) surfaces of all samples. In addition, the $SE42_R$ sample was analyzed following two short Ar-ion sputter cycles to remove surface carbon contamination and a portion of the outer film material.

The presence of C, Nb, O, Al, and Se was identified in the survey spectra of all samples; additionally, P and Cr were detected on the PAA-free surfaces. Narrow-scan C 1s, Nb 3d, O 1s, Al 2p, and Se 3d spectra were collected to analyze their core levels and bonding states. The experimental and fitted Nb 3d, Al 2p, and Se 3d spectra for the as-received surfaces are shown in Fig. 4. The corresponding spectra for the Ar-ion-sputtered $SE42_R$ film are presented in Fig. S10.

Fig. 4a shows the *Nb 3d spectrum* of the $SE42_A$ surface. Three doublets of appropriately constrained peaks are used to fit the spectrum (Nb $3d_{5/2}$ and $d_{3/2}$ with the fixed peak-separation energy of 2.75 eV, the fixed intensity ratio of 3:2, and the full width at half maximum (FWHM) equal for oxide components) [13]. The highest binding-energy (BE) doublet (Nb $3d_{5/2}$ at 206.85 eV) is due to Nb^{5+} cations in the oxide [13]. The lowest BE doublet (Nb $3d_{5/2}$ at 201.2 eV) of a comparable intensity is associated with metallic Nb^0 that separates the nanogoblets' bases

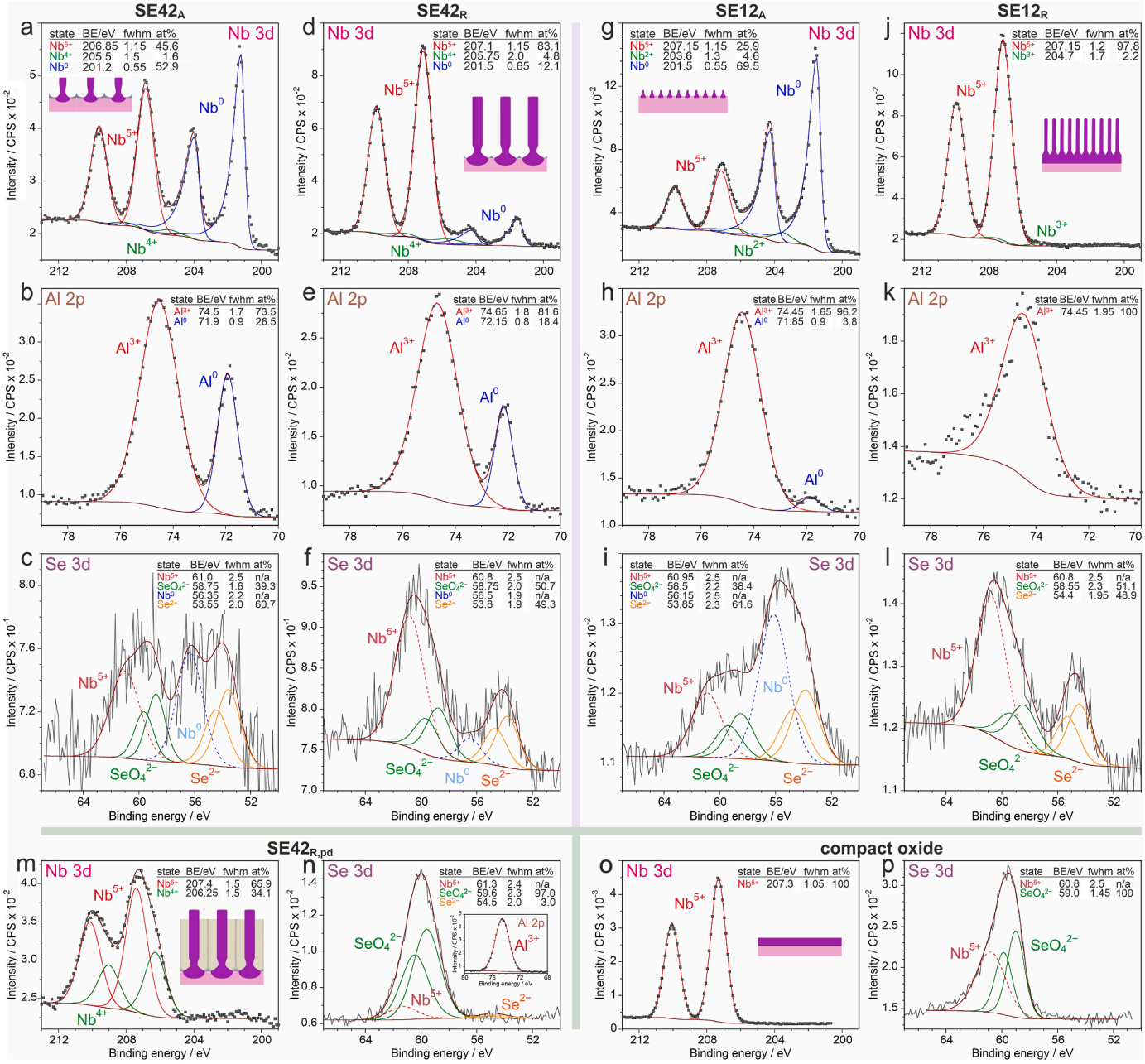

Fig. 4. Experimental and curve-fitted narrow-scan (first row) Nb 3d, (second row) Al 2p, and (third row) Se 3d XP spectra of PAA-free (a–c) $SE42_A$, (d–f) $SE42_R$, (g–i) $SE12_A$, (j–l) $SE12_R$ surfaces. (m) Nb 3d, (n) Se 3d, and (n-inset) Al 2p XP surface spectra of $SE42_R$ sample having partially-dissolved PAA layer. (o) Nb 3d and (p) Se 3d XP surface spectra of a compact niobium-oxide film prepared for comparison by anodizing niobium at 10 V in 1.5 M selenic acid.

(Fig. 2a–c). The amount of metallic Nb^0 is assessed as 53% of all Nb species. The third, lowest-intensity doublet, shifted to −1.35 eV from the Nb^{5+} component (with Nb $3d_{5/2}$ at 205.5 eV), is due to the presence of Nb^{4+} cations in the film, with a Nb^{5+}:Nb^{4+} ratio of 97:3. Due to the high amount of Nb^{5+} cations and the low amount of Nb^{4+} cations in the surface composition, the outmost film layer is assessed as stoichiometric Nb_2O_5 mixed with a minor amount of oxygen-deficient niobia.

The Nb 3d spectrum of the $SE42_R$ surface (Fig. 4d) is fitted with three doublets (with Nb $3d_{5/2}$ at 207.1, 205.75, and 201.5 eV), which are similarly associated with Nb^{5+}, Nb^{4+}, and Nb^0 species. The Nb^{5+}:Nb^{4+} ratio is 95:5, close to that of the $SE42_A$ surface. Therefore, the $SE42_R$ nanorods also contain substoichiometric (oxygen-deficient) niobium pentoxide. The amount of Nb^0 at the $SE42_R$ surface is much lower than that at the $SE42_A$ surface (12% vs. 53% of all Nb species). The two-times sputtering of the sample surface with weak-energy Ar ions (Fig. S10) reduces the contribution of Nb^0 from 12 to 8%. This means that a portion of the outer material was sputtered away along with the carbon contamination. Sputtering also changes the Nb^{5+}:Nb^{4+} ratio to 93:7 by increasing the amount of Nb^{4+} cations, which may be attributed to preferential oxygen sputtering. The presence of Nb^{4+} cations (and lower-oxidation-state metal cations in general) at the surface layer is a common phenomenon for the oxides formed by PAA-assisted anodizing [13,38,39].

The Nb 3d spectrum of the $SE12_A$ surface (Fig. 4g) is fitted with three doublets (Nb $3d_{5/2}$ at 207.15, 203.6, and 201.5 eV), the high- and low-BE doublets being due to Nb^{5+} and Nb^0. The amount of metallic niobium is relatively higher in this sample (70% of all Nb species). The lowest-intensity doublet shifted to −3.55 eV from the Nb^{5+} peak is assigned to Nb^{2+} cations in the anodic oxide [13]. The Nb^{5+}:Nb^{2+} ratio is 85:15, indicating the presence of stoichiometric Nb_2O_5 mixed with a relatively high amount of NbO suboxide.

The spectrum of the $SE12_R$ surface (Fig. 4j) consists of a high-intensity doublet with BE of 207.15 eV for Nb $3d_{5/2}$ associated with Nb^{5+} cations and a low-intensity doublet with BE of 204.7 eV for Nb $3d_{5/2}$. The 2.45 eV distance between them indicates that the low-intensity doublet is due to Nb^{3+} cations in the oxide. As the Nb^{5+}:Nb^{3+} ratio is low (98:2), the low-intensity peak is associated with small amounts of Nb_2O_3 suboxide mixed with Nb_2O_5. No metallic niobium species are detected at the $SE12_R$ surface. The high degree of oxide stoichiometry and the lack of metallic Nb on the surface may favor the application of such film as dielectric, which will be considered in Section 3.6.2.

The Nb 3d spectrum of the $SE42_{Rpd}$ surface (Fig. 4m) is fitted with two doublets (Nb $3d_{5/2}$ at 207.4 and 206.25 eV), associated with Nb^{5+} and Nb^{4+} cations, respectively. The lower-intensity peak, shifted to only −1.15 eV from the Nb^{5+} one, may be due to a more substoichiometric Nb_2O_5 owing to oxygen vacancies [40]. Since only the upper 40 nm-long parts of the rods are exposed for analysis (the lower parts of the rods are still covered by the remaining portion of PAA, as shown in the inset of Fig. 4m), the decreased Nb^{5+}:Nb^{4+} ratio of 66:34 indicates that the apexes of the nanorods contain a substantial amount of reduced oxide. This implies that the niobium oxide becomes relatively more reduced towards the upper parts of the rods. As expected, no metallic Nb is detected because the PAA layer covers the metallic residues between the rods' bases.

For comparison, the Nb 3d spectrum of the compact niobium-oxide surface is shown in Fig. 4o. A single doublet reproduces the spectrum with Nb $3d_{5/2}$ at 207.3 eV attributed to Nb^{5+} cations. The surface layer of the compact anodic niobium oxide is therefore composed of fully stoichiometric Nb_2O_5.

Summarizing the Nb 3d spectra analysis, the surfaces of the anodized and re-anodized nanostructures are predominantly composed of stoichiometric Nb_2O_5 mixed with a small portion of substoichiometric Nb_2O_5 (reduced or oxygen-deficient) or niobium suboxide (NbO or Nb_2O_3). The oxides could be mixed at the molecular level or present as nanoinclusions and unevenly distributed along the nanostructures. The most reduced oxide forms in the $SE12_A$ nanodots. Comparing the relative amount of the reduced oxide in the $SE42_R$ and $SE42_{Rpd}$ surfaces, we assume that the oxide substoichiometry increases toward the tops of the protrusions. All samples, except $SE12_R$, are confirmed to have metallic Nb separating the bases of the oxide nanostructures. The absence of Nb metal at the $SE12_R$ surface implies that the bases of the oxide nanorods fully merge to form a continuous bottom-oxide layer during re-anodizing, as also seen in the cross-fracture SEM images in Fig. 3f.

The *Al 2p spectra* of the $SE42_A$ and $SE42_R$ surfaces (Fig. 4b and e) are fitted with two single symmetrical peaks: The high-intensity peak is associated with Al_2O_3 (74.5 and 74.65 eV), and the low-intensity peak is due to metallic Al (71.9 and 72.15 eV). The metallic Al originates from the network of Al residues remaining around the niobium-oxide nanostructures over the metallic Nb (Fig. 2). After two times Ar-ion sputtering of the $SE42_R$ surface, the amount of metallic Al decreases from 18 to 13%, which indicates the removal of a thin surface layer. In the Al 2p spectrum of $SE42_{Rpd}$ (the inset in Fig. 4n), only the peak associated with Al_2O_3 is present (74.55 eV).

The Al 2p spectrum of the $SE12_A$ surface (Fig. 4h) is similarly fitted with a dominating peak assigned to Al_2O_3 (74.45 eV) and a lower-intensity peak assigned to metallic Al (71.85 eV). However, here the metallic contribution is substantially minor compared with the $SE42_A$ surface. This implies that aluminum remains at the $SE12_A$ surface in a substantially smaller amount than at the $SE42_A$ surface. The Al 2p spectrum of $SE12_R$ (Fig. 4k) has a single Al_2O_3-related peak (74.45 eV), indicating the absence of metallic Al.

The metallic contributions to the Nb 3d and Al 2p spectra originating from the corresponding metallic residues around the nanostructures' bases were subtracted from the overall content of the elements to obtain an approximate surface amount of Nb and Al in the oxides. For Al, the corresponding native oxide was also considered and subtracted [41]. Provided that at.%(Al + Nb) = 100%, the $SE42_A$ and $SE42_R$ nanostructures are estimated to have 65 and 61 at.% of Al, respectively, while the $SE12_A$ and $SE12_R$ counterparts show 81 and 47 at.% of Al, respectively. Therefore, the surface of the nanostructures is composed of mixed Nb_2O_5–Al_2O_3, whereas their interior is most likely alumina-free Nb_2O_5 [13]. Similarly, a large amount of surface Al (about 75 at.%) has previously been reported for the PAA-assisted N-doped TiO_2 nanocolumns [39].

The noisy *Se 3d spectra*, associated with the low Se concentration, and their overlapping with the Nb 4s peaks complicates the analysis of the Se 3d spectra. The presence of multiple components is assumed and confirmed by comparing the spectra of the various samples, fitting them, and verifying the peak positions with the literature-reported values: Nb 4s peak of Nb^{5+} cations, Nb 4s peak of Nb^0 atoms, Se 3d peaks of *selenate* anions (SeO_4^{2-}), and Se 3d peaks of *selenide* anions (Se^{2-}). A single peak of Nb 4s transition for Nb^{5+} was assumed at ~60.5 eV [42]. The Nb^0 line was assumed at ~56.0 eV [42]. The fitting leads to 60.9 ± 0.2 and 56.4 ± 0.1 eV for the Nb^{5+} and Nb^0 peaks, respectively. The area below the Nb 4s peaks was considered proportional to the area of the corresponding Nb 3d peaks (based on the relative sensitivity factors of 0.126 and 2.921 for Nb 4s and Nb 3d, respectively). However, the fitting results in the 2.0 ± 0.1-fold lower-intensity for Nb 4s peaks than theoretically expected. The area of the Nb^0 peak was constrained as a multiple of the Nb^{5+} peak to agree with the corresponding Nb 3d spectra. The Se 3d transitions were fitted as doublets with a constrained spin-orbit splitting of 0.86 eV [43], the ratio of the Se $3d_{3/2}$ and $3d_{5/2}$ components was fixed at 0.72 [43], and FWHMs were constrained to be equal within each component. The BEs of Se $3d_{5/2}$ peaks of ~60 eV and ~54.5 eV were expected for SeO_4^{2-} and Se^{2-} anions, respectively [43,44]. The fitted BEs of the Se $3d_{5/2}$ peaks are 58.55–59.6 (avg. 58.8) eV for the selenate and 53.55–54.5 (avg. 54.0) eV for the selenide ions, agreeing with the literature.

The Se 3d spectra are shown in the 3rd row of Fig. 4. They are all fitted with Nb 4s peaks for Nb^{5+} and possibly Nb^0, correlating with the corresponding Nb 3d spectra, and with two doublets of Se 3d peaks for

SeO_4^{2-} and Se^{2-} ions. Provided that at.%(SeO_4^{2-}+Se^{2-}) = 100%, the amounts of Se^{2-} anions are 61 at.% for the anodized ($SE12_A$ and $SE42_A$) and 49 at.% for the re-anodized samples ($SE12_R$ and $SE42_R$). After the two-times sputtering of the $SE42_R$ surface, the amount of Se^{2-} ions increases from 49 to 64 at.%. On the other hand, a dominating amount of SeO_4^{2-} ions is found in the Se 3d spectrum of the $SE42_{Rpd}$ sample (Fig. 4n), with only a minor contribution of Se^{2-} ions (~3 at.%). No selenides are assumed from the Se 3d spectrum of the compact niobium oxide (Fig. 4p), which is fitted only with one SeO_4^{2-} doublet (in addition to an Nb 4s peak of Nb^{5+}).

The peak area of Se 3d components (i.e., without the contribution of Nb 4s) was used to calculate the amount of Se at the sample surfaces (provided at.%(Al + Nb + Se) = 100%), after subtracting the metallic contribution from the Al 2p and Nb 3d spectra, as described above. The $SE42_A$ and $SE42_R$ surfaces have 5.3 and 3.2 at.% of Se, respectively, whereas the $SE12_A$ and $SE12_R$ surfaces have 3.9 and 4.9 at.% of Se, respectively. Sputtering the $SE42_R$ surface affects the Se content slightly (2.8 at.%). The $SE42_{Rpd}$ surface shows a little higher Se amount (4.3 at.%) than the PAA-free $SE42_R$. On the other hand, the surface of the compact niobium oxide has a substantially more considerable Se amount (9.6 at.%) relative to the nanostructured samples.

In summary, the chemical composition of the outmost nanostructures' material can be expressed as a mixture of Al_2O_3 and niobium oxides: stoichiometric Nb_2O_5 mixed with substoichiometric Nb_2O_5 or with a suboxide expressed on average as $NbO_{2.5}{\cdot}xNb^{n+}O_{n/2}$. A portion of the O^{2-} anions in both oxides is replaced by SeO_4^{2-} and possibly Se^{2-} anions, as summarized in Table 2. There is 47–81 at.% of Al_2O_3 at the sample surfaces, and about 1.5–3.0% of the O^{2-} anions are replaced by selenium species. The $SE42_{Rpd}$ surface contains much more alumina on average (95 at.%), apparently due to the presence of the PAA matrix surrounding the tops of the rods, and 2.9% of the O^{2-} anions are replaced by selenium species. Contrarily to the nanostructured surfaces, the compact anodic niobium-oxide film contains neither Al^{3+} nor Se^{2-} ions. It mainly comprises stoichiometric Nb_2O_5, in which 4.2% of the O^{2-} anions are replaced by SeO_4^{2-} anions.

3.5. Oxide growth model

3.5.1. Formation-morphology relationship

Based on the present experimental findings and with reference to previous publications [12–14], we developed a model for the PAA-assisted growth of nanostructured niobium-oxide-based ceramic nanoarrays in the selenic-acid electrolyte, as sketched in Fig. 5. The growth steps depicted in Fig. 5 correspond to the film-formation stages in Fig. 1: (a and f) the steady-state PAA growth during the 1st stage, (b and g) the anodizing of the Nb underlayer during the 2nd stage, and (c and h) the re-anodizing of the Nb underlayer during the 3rd stage.

Initially, the upper Al layer is anodized [45] at the high (42 V) or low (12 V) steady-state voltages. The SeO_4^{2-} electrolyte-derived anions are incorporated in the growing PAA. A small portion of the PAA at the barrier layer/aluminum interface, about 10% of the barrier-layer thickness, typically remains impurity-free [45,46]. When the PAA cells touch the Nb metal, niobium oxide begins to grow inside the PAA barrier layer, accompanied by the partial dissociation of the Al–O bonds under the high electric field, which is typical for some other valve metals [47–49]. Nanochannels of niobium oxide grow within the PAA barrier layer via the cross-migration of cations and anions. Finally, the growing oxide protrudes into the pores, and the nanochannels within the PAA barrier layer expand to form solid niobium-oxide bulges (Fig. 5b and g). The oxide also grows within the PAA cell walls due to the enhanced ionic transport through various defects in the outer cell-wall material: the incorporated electrolyte species, structural imperfections, vacancies, etc. [13]. Due to this phenomenon, the niobium-oxide nanostructures grow thicker than the PAA pores, and a mixed alumina-niobia region forms along the Nb_2O_5/Al_2O_3 interface. The anodizing of the underlying Nb competes with the anodizing of the residual Al network surrounding the bottoms of the PAA cells. The Al residues may remain after completing the anodizing step or may be fully oxidized – the behavior depends upon the ratio of the ionic resistivities of anodic alumina and niobia.

Re-anodizing to a higher voltage (Fig. 5c,h) results in proportionally elongating and thickening the niobium-oxide protrusions, further filling the pores and occupying more space within the PAA cell walls. New niobium oxide also keeps growing beneath the PAA cells due to the O^{2-} migration. The nanorods' bases expand and deepen but do not merge in $SE42_R$ (Fig. 5c). However, they merge into a continuous bottom-oxide layer in $SE12_R$ (Fig. 5h).

The different manners of the bottom-oxide growth in $SE42_A$-$SE42_R$ and $SE12_A$-$SE12_R$ pairs arise from dissimilar ionic resistivities of the two types of niobium-oxide nanoprotrusions. The higher the ionic resistivity of the anodic niobium oxide (closer to that of alumina), the more the bottom oxide expands under the pores. The differences in the niobium-oxide resistivities are mostly related to the variations in chemical compositions and dissimilar alumina-niobia mixing within the PAA barrier layer and cell walls. The second practically essential and closely related phenomenon is the presence or absence of unoxidized aluminum after completing the anodizing and re-anodizing stages. The ionic resistivities of the $SE12_A$ and $SE12_R$ niobium-oxide nanoprotrusions are higher than those of the $SE42_A$ and $SE42_R$ nanoprotrusions since only small traces of residual Al metal remain in $SE12_A$, while $SE12_R$ is entirely Al-free. Oppositely, the relatively lower resistivity of the $SE42_A$ and $SE42_R$ niobium-oxide nanoprotrusions results in more aluminum remaining around the protrusions.

Notably, the ionic resistivity of the Nb_2O_5 nanostructures can be controlled by adjusting the anodizing process parameters and may be considered for engineering niobium-oxide nanoarrays for particular applications. It is possible to modulate the residual Al network on the sample surface to merge the nanostructures' bases into a continuous Nb_2O_5 bottom layer. For applications of the free-standing Nb-metal-supported Nb_2O_5 nanostructures without any traces of Al metal, a NaOH

Table 2
Surface chemical composition of the niobium-oxide nanostructures formed via the PAA-assisted anodizing/re-anodizing in 1.5 M selenic acid.

	Substoichiometric niobium pentoxide[a] $NbO_{2.5}{\cdot}xNb^{n+}O_{n/2}$		Al:Nb ratio	Related to Se		
				at.% of Se (Se + Al + Nb = 100 at.%)	% of O^{2-} replaced by Se species	SeO_4^{2-}: Se^{2-}
	n	x				
$SE42_A$	4	0.034	65:35	5.3	3.0	39:61
$SE42_R$	4	0.057	61:39	3.2	1.8	51:49
$SE42_R$ after 1st sputtering	4	0.074	63:37	2.8	1.5	40:60
$SE42_R$ after 2nd sputtering	4	0.081	62:38	2.8	1.5	36:64
$SE42_{Rpd}$	4	0.52	95:5	4.3	2.9	97:3
$SE12_A$	2	0.18	81:19	3.9	2.5	38:62
$SE12_R$	3	0.024	47:53	4.9	2.6	51:49
compact niobium oxide	n/a	n/a	0:100	9.6	4.2	100:0

[a] The outer material of the nanostructures was expressed as a mixture of Al_2O_3 with niobium oxides (stoichiometric Nb_2O_5 mixed with substoichiometric Nb_2O_5 or with a suboxide, in average $NbO_{2.5}{\cdot}xNb^{n+}O_{n/2}$), in which some of the O^{2-} anions are replaced by SeO_4^{2-} (selenate) and Se^{2-} (selenide) anions.

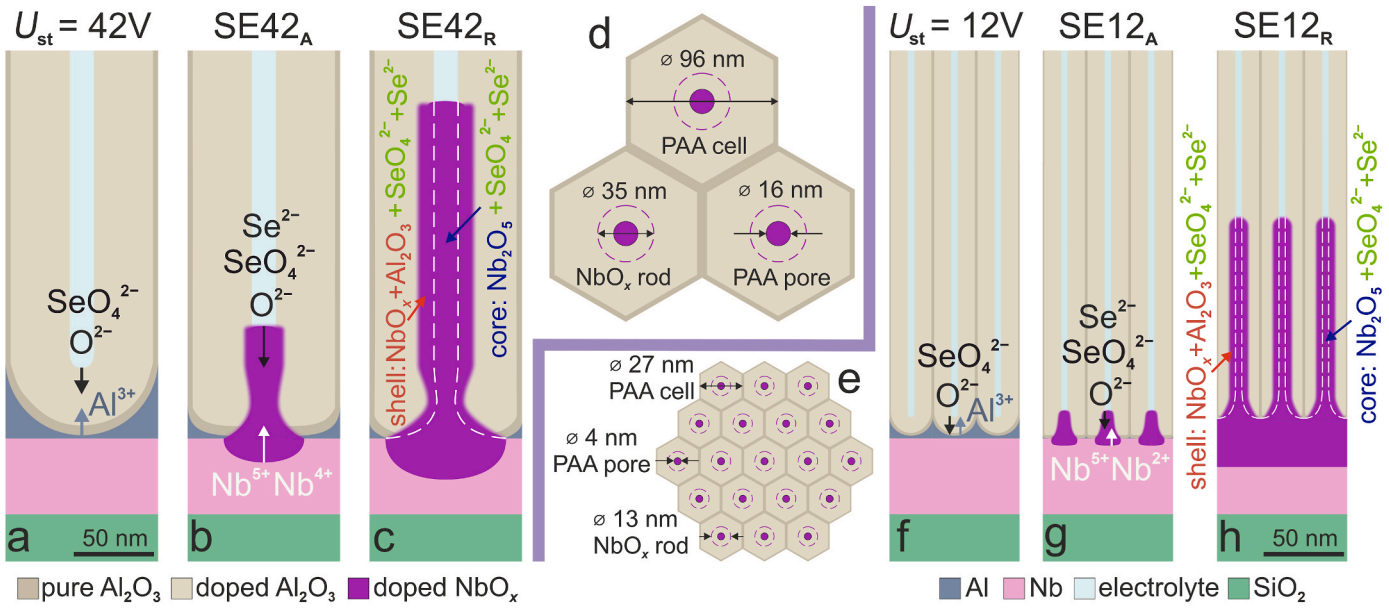

Fig. 5. Schematic growth model during the PAA-assisted anodizing and re-anodizing of niobium in 1.5 M selenic acid for forming (left panel) SE42$_A$ (42 V) and SE42$_R$ (120 V) samples and (right panel) SE12$_A$ (12 V) and SE12$_R$ (80 V) samples: (a and f) the formation of PAA layer (1st stages in Fig. 1 just before the voltage begins to increase), (b and g) the growth of niobium-oxide nanostructures within the PAA barrier layer during the anodizing (2nd stages in Fig. 1), and (c and h) the development of niobium-oxide nanorods during the re-anodizing (3rd stages in Fig. 1). The dashed white lines differentiate the 'core/shell' structure of the protrusions. The parallel-to-substrate section views show comparatively the cell-pore-rod relationship for (d) SE42$_R$ and (e) SE12$_R$ samples.

etchant may be used to dissolve both the PAA and the remaining Al. Additionally, after dissolving the PAA and/or the remaining Al, the unoxidized Nb metal surrounding the nanorods may be anodized and transformed into a continuous compact Nb_2O_5 layer of a desired thickness, as described elsewhere [50].

3.5.2. *Ionic transport and oxide growth*

Another essential feature that should be considered is the incorporation of SeO_4^{2-} (selenate) and Se^{2-} (selenide) anions in the nanoarrays. The SeO_4^{2-} anions are present in the anodizing electrolyte because of the complete dissociation of H_2SeO_4. These ions adsorb on the anode surface and migrate inward under the high electric field during the anodizing and re-anodizing (with a slower rate relative to O^{2-} (OH^-) anions). The following anode reactions express the niobium-oxide formation and selenate-ion incorporation:

$$2Nb^{5+} + 5O^{2-} \rightarrow Nb_2O_5 \quad (2)$$

$$2Nb^{5+} + 5(1-y_1)O^{2-} + 5y_1SeO_4^{2-} \rightarrow Nb_2O_{5(1-y1)}(SeO_4)_{5y1} \quad (3)$$

where coefficient y_1 represents the fraction of O^{2-} anions replaced by selenate anions in the niobium oxide.

The incorporation of selenide, or possibly hydrogen selenide (HSe^-) anions [51,52], in the outer nanostructures' layer occurs after such anions form in the selenic-acid electrolyte of the given concentration and the corresponding pH due to the reduction of selenate anions on the cathode via a series of step reactions:

$$SeO_4^{2-} + 3H^+ + 2e^- \rightarrow HSeO_3^- + H_2O \text{ [51,52,53]} \quad (4)$$

$$HSeO_3^- + 5H^+ + 4e^- \rightarrow Se^0 + 3H_2O \text{ [51,52,53]} \quad (5)$$

$$HSeO_3^- + 6H^+ + 6e^- \rightarrow HSe^- + 3H_2O \text{ [51]} \quad (6)$$

$$Se^0 + H^+ + 2e^- \rightarrow HSe^- \text{ [51,52]} \quad (7)$$

Reactions (4–7) can be summarized by the following overall cathode reaction:

$$SeO_4^{2-} + 9H^+ + 8e^- \rightarrow HSe^- + 4H_2O \quad (8)$$

The reduction of the negatively charged species at the cathode is enabled by the diffusion of anions from the bulk electrolyte across the Helmholtz layer, as explained elsewhere [54]. A red powder, presumably elemental Se, is observed on the cathode during the anodizing/re-anodizing. Considering the 3-mm distance between the electrodes in the anodizing setup, the formed selenide anions are expected to be transported from the cathode to the anode by diffusion within a few minutes, which happens already during the growth of the PAA overlayer. The fact that selenide anions are incorporated in the PAA-assisted niobium oxides (Fig. 4c,f,i,l) but are not present in the compact niobium oxide (Fig. 4p) confirms that the selenide anions did not diffuse toward the compact niobium oxide before its growth was finished (within ~2 min after applying the polarization). However, since the PAA-assisted niobium-oxide nanoarrays only start to grow after the PAA overlayer is fully formed, a substantial amount of selenide anions is already produced at the cathode. These selenide anions have enough time to diffuse toward the anode and enter the preformed PAA pores well before the beginning of anodizing and, especially, re-anodizing the niobium underlayer. Assuming that HSe^- anions drop their protons at the anodic-oxide surface before the migration, the following anode reaction summarises the incorporation of selenide anions into the nanostructured niobium oxide:

$$2Nb^{5+} + 5(1-y_2)O^{2-} + 5y_2Se^{2-} \rightarrow Nb_2O_{5(1-y2)}Se_{5y2} \quad (9)$$

where coefficient y_2 represents the fraction of O^{2-} anions replaced by selenide anions in the anodic niobium oxide. The sum of y_1 and y_2 in reactions (3) and (9) corresponds to the fraction of O^{2-} anions in the oxide replaced by all-type Se species, similar to the values summarized in Table 2 as the percentages. Anode reactions (3) and (9) can be summarized by the following overall reaction for the PAA-assisted niobium-oxide growth in selenic acid:

$$2Nb^{5+} + 5(1-y_1-y_2)O^{2-} + 5y_1SeO_4^{2-} + 5y_2Se^{2-} \rightarrow Nb_2O_{5(1-y1)}(SeO_4)_{5y1}Se_{5y2} \quad (10)$$

Conclusively, the experimental findings of this work suggest that the nanostructured ceramics formed via the PAA-assisted selenic-acid niobium anodizing have a dual (core/shell) composition: the inner

material (the core) is stoichiometric Nb_2O_5, whereas the outer layer (the shell) is a few nm-thick substoichiometric NbO_x mixed with Al_2O_3. The arrays grow doped with selenate and selenide anions originating from the electrolyte and capable of migrating inward under the high electric field.

3.6. Prospective applications

3.6.1. Substrates for SERS biosensing

Surface-enhanced Raman spectroscopy (SERS) has emerged as a powerful spectroscopic technique for label-free chemical identification of biomolecules. However, the widespread adoption of SERS is hindered by the high cost, poor biocompatibility, and instability of commercially available nanostructured SERS noble-metal substrates [55]. These drawbacks motivate researchers to develop alternative materials and engineer their surfaces to pursue novel substrates for SERS applications. Generally, nanostructured Nb_2O_5 ceramics could be an option to substitute noble metals due to the oxide's attractive properties for SERS application [56].

Tunability of the nano-morphology is the key to SERS application since SPR is the main contributor to Raman spectra enhancement. It depends on the oxide nanostructures' specific geometry, structure, size, and relative position [56]. The PAA-assisted anodizing can be a potent tool for fabricating nanostructured Nb_2O_5 ceramic substrates suitable for SERS due to the tunability of the surface morphology (Figs. 2 and 3) and the cost efficiency of the formation method. However, anodizing is commonly not considered for synthesizing nanostructured SERS substrates as incorporated electrolyte-derived species often alter the Raman response and hinder SERS signals. Various organic, phosphate, or fluoride species can cause the substrate's background fluorescence and mask SERS signals due to the fundamental intersection of fluorescence with Raman scattering [27]. However, selenic-acid aluminum anodizing was previously noted as a way to produce fluorescence-free PAA films [25]. Therefore, it is highly anticipated that the PAA-assisted selenic-acid niobium anodizing may help achieve the Nb_2O_5 ceramic nanoarrays without the unwanted spectral contamination caused by the electrolyte species.

Further, we explored the impact of the incorporated electrolyte species on the PL and Raman spectra of the PAA-assisted Nb_2O_5 nanorods. The PAA-free $SE12_R$ film was compared with the PAA-free $OX12_R$ film. The PL emission spectra recorded under the same setup for both samples are shown in Fig. 6a. The $SE12_R$ film exhibits a weak PL band without a pronounced emission peak. Contrarily, the $OX12_R$ film produces a noticeably higher PL emission with an intensive PL band over the blue region. The $OX12_R$ PL spectrum resembles the blue PL emission previously reported for PAA synthesized in oxalic acid [57]. Therefore, the PL emission from the $OX12_R$ film most likely originates from the incorporated oxalate anions [58].

Fig. 6b compares Raman scattering from the PAA-free $SE12_R$ and $OX12_R$ films. The $OX12_R$ spectrum does not exhibit any characteristic bands. Instead, a fluorescent halo completely masks the Raman signal. Similar masking of the Raman spectrum was previously reported for PAA formed in oxalic acid and can be related to fluorescence from the oxalic-acid impurities in the oxide [25]. In contrast, the $SE12_R$ spectrum is free from any spectral contaminants. Two characteristic bands are distinguished at 660 and 900 cm^{-1}. Both bands are attributed to Nb–O vibrations [59,60]. The spectrum does not contain any additional bands or fluorescence noise. Above 1000 cm^{-1}, the spectrum only includes a baseline signal clear of any spectral additions.

The PAA-assisted selenic-acid niobium anodizing can lead to various niobium-oxide nano-morphologies: from the short-distanced sub-10 nm nanodots to the well-separated and substantially longer oxide nanorods. This feature can help modulate SPR to achieve the desired enhancement of the Raman signal. Notably, the incorporated selenium species do not contribute to PL emission nor hinder the Raman signal of the substrate. Thus, the high tunability of the oxide morphology, the lack of PL emission, and the absence of interferences to the Raman spectra make the PAA-assisted selenic-acid niobium anodizing a promising tool to fabricate novel Nb_2O_5 nanoceramic substrates for SERS applications. Additionally, the tendency to agglomerate may help form 3D-distributed high-density hot spots, generating a highly enhanced localized electromagnetic field to amplify the Raman signal and increase the detection limit [61]. The impact of various morphologies of the Nb_2O_5 ceramic nanoarrays on the Raman signal enhancement will be explored in future work.

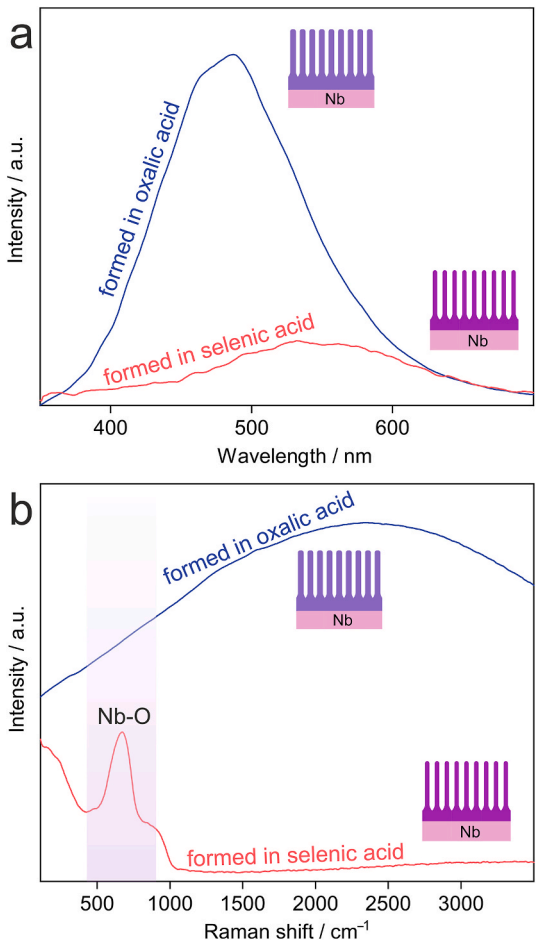

Fig. 6. Comparative (a) photoluminescence and (b) Raman spectra of the PAA-assisted niobium-oxide nanoarrays synthesized in 1.5 M selenic acid and 0.6 M oxalic acid under the same formation voltages: anodizing at $U_{st} = 12$ V followed by re-anodizing to 80 V.

3.6.2. Capacitor dielectrics

Alloying, laminating, or periodically mixing high-permittivity Nb_2O_5 with medium-permittivity Al_2O_3 may result in composite films with enhanced dielectric properties and improved reliability [62]. Drawing inspiration from the advanced dielectric performance of the Al_2O_3–Ta_2O_5 and Al_2O_3–ZrO_2 electroceramics synthesized in our previous works [63–65], we fabricated an experimental MIM device utilizing for the first time the planar PAA-embedded Nb_2O_5 nanorods synthesized in the selenic acid, as described in the Experimental section. Incorporating Se species in the niobium-oxide nanostructures and the exceptionally thin PAA nanopores were expected to effectively suppress niobium-oxide crystallization and promote a transition from semiconductor to dielectric properties.

Due to the nearly perfect $SE12_R$ stoichiometry and the absence of Nb and Al metallic residues at the Al_2O_3/Nb_2O_5 interface, the planar nanocomposite anodic-oxide film was fabricated under the $SE12_R$

formation conditions. The challenge with the planar film was to grow the PAA-embedded Nb_2O_5 nanorods traversing the PAA layer up to the top. Not having the empty pores above the niobium-oxide nanorods was considered crucial for advancing the dielectric performance of the anodic film and making the anodizing technique compatible with multilayer microfabrication technologies.

Fig. 7 shows SEM images and a schematic outline of the capacitor dielectric and the assembled MIM device. From Fig. 7a and b, the PAA pores are fully filled with the niobium-oxide nanorods, resulting in a ~110 nm-thick Al_2O_3–Nb_2O_5 mixed-oxide layer. This layer resides on a continuous ~30 nm-thick bottom niobium-oxide layer. Together both layers constitute a laminated nanocomposite mixed-oxide electroceramic dielectric with an effective (total) thickness of 140 nm (Fig. 7c and d).

Fig. 8a shows the Bode plot for the MIM device recorded at room temperature in the 10^2–10^6 Hz range. A combination of the linear decline of the impedance modulus with a −1 slope and the phase shift approaching −90° indicates the nearly ideal dielectric behavior of the anodic film. The apparent relative permittivity, ε_r, calculated from the Bode plots, is ~18, which differs from the known permittivities of Nb_2O_5 (~35) and Al_2O_3 (~9) [66]. A unique ε_r arises from the laminated and nanocomposite film architecture: the Nb_2O_5 nanostructures embedded in, and partially mixed with, the PAA cell walls, superimposed on the Nb_2O_5 bottom layer. The apparent ε_r of the Al_2O_3–Nb_2O_5 mixed-oxide ceramic (~18) is substantially higher than ε_r of recently reported Al_2O_3–ZrO_2 nanocomposite dielectric (~11) synthesized via the PAA-assisted re-anodizing of Zr metal [65]. The increased film permittivity underlines the advantages of the Se-doped Nb_2O_5–Al_2O_3 nanocomposite ceramic layers as a high-*k* dielectric for MIM capacitors. More generally, the device performance confirms the dielectric nature of the mixed-oxide film.

The ε_r is interrelated with the capacitance density of the device, *C*. Therefore, both values slightly decline with increasing frequency (Fig. 8b and the inset); the behavior being typical for ceramic capacitors. As seen in Fig. 8b, the device exhibits a systematically low ~1×10^{-2} loss tangent, tan δ, in the 10^2–10^5 Hz frequency range, which further drops to 2×10^{-4} with increasing frequency to 10^6 Hz. Such an extraordinarily low tan δ for ceramic materials at frequencies over 10^5 Hz might be due to incorporated Se species, which may stabilize the amorphous mixed-oxide composition and substantially prolong the relaxation time at room temperature.

The major drawback of pure Nb_2O_5 ceramics for capacitor applications is the crystalline nature and narrow band gap of the oxide (~3.4 eV), which inevitably gives rise to semiconductor properties and high leakage currents [67]. In our work, we expected to solve the problem by incorporating Se-doped amorphous Nb_2O_5 nanorods into the dielectric PAA matrix. Fig. 8c shows the leakage current density, *J*, against the bias voltage, *V*, of the test MIM device. The device exhibits as low *J* as 16 nA cm^{-2} at 15 V bottom-electrode injection and 18 nA cm^{-2} at 15 V top-electrode injection. Such a low leakage-current density is most likely related to the contribution of the amorphous PAA matrix having a band gap of ~7.0 eV [68]. Additionally, suppressing the crystallization of Nb_2O_5 in the sub-10 nm PAA pores eliminates leakage paths through the oxide grain boundaries. The low leakage current achieved in the present work complements the findings of previous works on laminating or mixing inorganic metal oxides with Al_2O_3 to improve the capacitor leakage-current characteristics [69,70].

3.6.3. Superhydrophobic coating

The PAA-assisted selenic-acid anodizing can be practical to populate large surfaces with vertically aligned, well-distanced, and super-thin Nb_2O_5 ceramic nanorods. Modifying such surfaces with a monolayer of low-surface-energy molecules may result in the water droplets residing merely on the apexes of nanostructures and a cushion of trapped air. Air trapping is crucial for achieving a high water contact angle (WCA) and accomplishing superhydrophobic properties (WCA>150°) of the ceramics. The Cassie-Baxter equation governs a wetting regime with the trapped air [71]:

$$\cos\theta^* = -1 + f_s(1 + \cos\theta) \quad (11)$$

where θ^* is the WCA for a nanostructured surface, f_s is the fraction of the solid in contact with the liquid (identical to the projection of nanostructures' diameters $A/100$), and θ is the equilibrium WCA for a smooth uniform Nb_2O_5 surface.

From Eq. (11), high θ^*>150° can be achieved by lowering f_s via adjusting the surface morphology and increasing θ via a surface modification to reduce the intrinsic surface affinity for water. Although there is a fundamental limit for increasing θ due to polar and van der Waals liquid-solid interactions, the f_s-value can be effectively reduced by selecting an appropriate surface nanostructuring method. The f_s is calculated similarly to *A* (Table 1) and is, therefore, proportional to d_n and D_{cent}. The small d_n and large D_{cent}-values of the Nb_2O_5 nanostructures formed in the selenic acid open the way for lowering f_s and improving the surface water repellency. For example, the $SE42_A$ nanogoblets yield ~0.06 f_s, which is 1.5-fold lower than ~0.09 f_s for the $OX42_A$ nanogoblets. It is anticipated that f_s may be lowered even further by adjusting the formation conditions and electrolyte concentration [24]. The lower f_s, the lack of oxide coloration, and the high optical transparency of the Nb_2O_5-based ceramic nanoarrays formed in the selenic acid could be instrumental in creating advanced self-cleaning optical coatings for intelligent windows, solar cell passivation, or display devices [24,72,73]. Experimental justification of these suggestions will be provided in future works.

3.6.4. Biomedical coatings

Nb_2O_5-based ceramics have recently emerged as novel biomedical coatings. Reportedly, they can improve living-cell viability, adhesion, proliferation, and differentiation while suppressing inflammation and

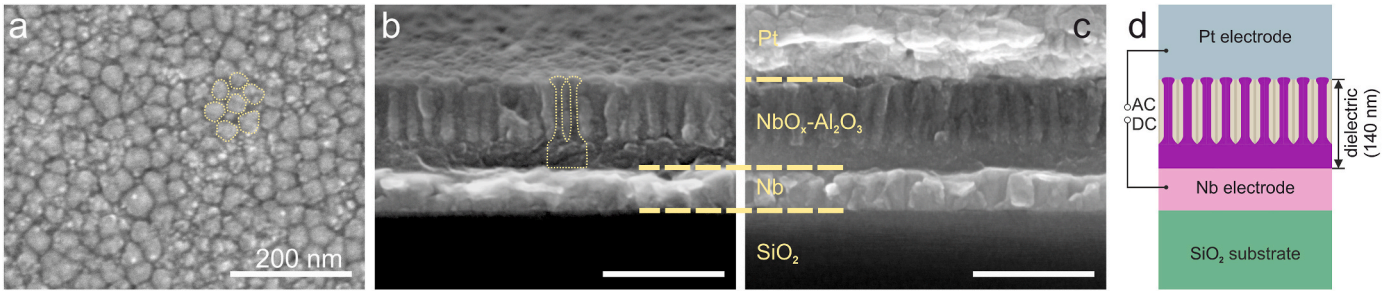

Fig. 7. Thin-film MIM capacitor based on the planar Nb_2O_5–Al_2O_3 nanocomposite dielectric via the PAA-assisted selenic-acid anodizing of niobium at 12 V followed by re-anodizing to 70 V: (a) SEM surface view of the capacitor dielectric, and (b) SEM cross-fracture views depicting the dielectric on the bottom niobium-metal electrode; (c) SEM cross-fracture view of the capacitor after the deposition of the top electrode, (d) schematic view of the assembled capacitor. All undefined scale bars are 200 nm.

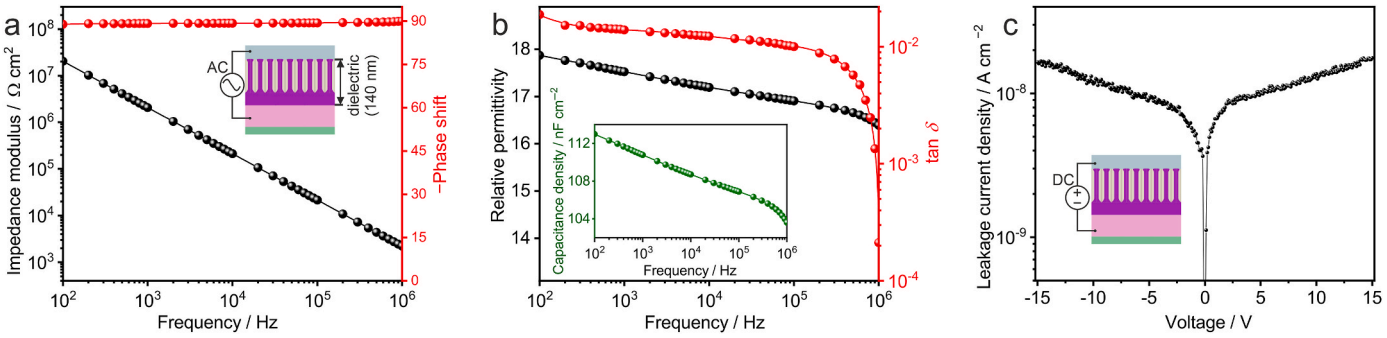

Fig. 8. Electrical performance of the MIM capacitor at room temperature: (a) the Bode plots, (b) the relative dielectric permittivity and the loss tangent vs. frequency (the inset shows the capacitance density vs. frequency), and (c) the leakage-current density vs. DC bias voltage.

infections by inhibiting bacteria growth [28]. Surface nanopatterning via PAA-assisted anodizing is a facile method to enhance biomedical characteristics of ceramics, as was previously noted for the PAA-assisted nanostructured Ta_2O_5, ZrO_2, and HfO_2 [74–76]. The PAA-assisted selenic-acid anodizing can be used not only to nanopattern Nb_2O_5 ceramics but additionally to incorporate biomedically potent Se-species into oxide structure (Fig. 4).

For utilizing the Nb_2O_5 ceramic nanoarrays (Figs. 2 and 3) in biomedicine, the amount of incorporated Se species should be carefully balanced due to the high intrinsic toxicity of Se and its ability to impair cell functions [77]. However, Se species in small concentrations do not interfere with the cell lifecycle. They can instead serve as potent antioxidants to enhance surface antibacterial activity and even introduce novel anti-oncogenic properties [78]. The compact anodic niobium-oxide film prepared by conventional anodizing in H_2SeO_4 electrolyte yields a 2.7 at. % surface concentration of the incorporated Se (Fig. 4p), which can render it unsuitable for biomedical applications due to a high level of selenium-induced toxicity. In contrast, the PAA-assisted selenium-acid anodizing results in a higher surface-to-volume ratio but relatively lower Se surface concentration, which can be tuned from 1.1 to 1.9 at.% by adjusting the anodizing parameters. Additionally, the amount of surface Se in the niobium-oxide nanostructures can be altered by adjusting the electrolyte concentration. Biocompatibility of the Se-doped PAA-assisted niobium-oxide nanoceramics will be the subject of future research.

3.6.5. Catalysts and gas sensors

The facile fabrication of Nb_2O_5 nanostructured ceramics with a high surface-to-volume ratio is an essential milestone for advancing catalytic and gas-sensing applications of the oxide [4,30,79]. The Nb_2O_5 ceramic nanoarrays formed via the PAA-assisted selenic-acid anodizing are expected to have a dramatically increased active surface (Fig. 3d and e) compared with a flat Nb_2O_5 surface. Therefore, such niobium-oxide nanostructures are potent for increasing the number of active sites capable of reacting with gas molecules. The electrochemical approach developed here, combined with standard microfabrication technologies, can help achieve Nb_2O_5-based gas sensors having improved sensitivity and selectivity. The large surface-to-volume ratio associated with the PAA-assisted Nb_2O_5 ceramic nanoarrays may also be highly suitable for catalytic applications. In addition to the structural benefits, the Nb_2O_5 nanoceramic catalysts may benefit from the incorporated Se species, which can reportedly enhance the material's reactivity and selectivity [80].

4. Summary and conclusions

1. Arrays of upright-standing spatially-separated protrusions shaped as nanodots (9–20 nm), nanogoblets (24–75 nm), and nanorods (13–210 nm) were created via the PAA-assisted anodizing of niobium in selenic acid. The nanostructures are 1.3-fold thinner and exhibit a 1.5-fold smaller projection area than the reference nanostructures formed via the PAA-assisted anodizing of niobium in oxalic acid.
2. The nanostructures have a core/shell composition: the core is stoichiometric Nb_2O_5, whereas the shell is a several-nm-thick sub-stoichiometric NbO_x mixed with Al_2O_3. The PAA-assisted niobium-oxide nanoarrays grow doped with selenate (SeO_4^{2-}) and selenide (Se^{2-}) anions originating from the electrolyte and migrating inward under the high electric field. Selenium species at the outmost shell surface replace 1.5–3.0% of the O^{2-} ions depending on the formation conditions.
3. Potential applications of the Nb_2O_5–Al_2O_3 composite ceramic nanoarrays are as novel Nb_2O_5-based SERS substrates, advanced dielectric layers for thin-film capacitors, and highly promising self-cleaning, optical, biomedical, antibacterial, gas-sensing, or catalytic coatings.

Declaration of competing interest

The authors declare that they have no known competing financial interests or personal relationships that could have appeared to influence the work reported in this paper.

Acknowledgments

This research was supported by a grant from the Czech Science Foundation (GA ČR) no. 20-25486S. CzechNanoLab project LM2018110 funded by MEYS CR is acknowledged for the financial support of silicon wafer oxidation, magnetron sputter-deposition, SEM, and electric/dielectric measurements at CEITEC Nano Research Infrastructure. EL was supported by the Catalan Institution for Research and Advanced Studies via the 2018 Edition of the ICREA Academia Award, Catalonia, Spain.

Appendix A. Supplementary data

Supplementary data to this article can be found online at https://doi.org/10.1016/j.ceramint.2023.08.134.

References

[1] K. Nakajima, Y. Baba, R. Noma, M. Kitano, J.N. Kondo, S. Hayashi, M. Hara, $Nb_2O_5 \cdot nH_2O$ as a heterogeneous catalyst with water-tolerant Lewis acid sites, J. Am. Chem. Soc. 133 (2011) 4224–4227, https://doi.org/10.1021/ja110482r.
[2] A. Mozalev, H. Habazaki, J. Hubálek, The superhydrophobic properties of self-organized microstructured surfaces derived from anodically oxidized Al/Nb and Al/Ta metal layers, Electrochim. Acta 82 (2012) 90–97, https://doi.org/10.1016/j.electacta.2012.05.065.
[3] P. Amaravathy, S. Sowndarya, S. Sathyanarayanan, N. Rajendran, Novel sol gel coating of Nb_2O_5 on magnesium alloy for biomedical applications, Surf. Coat. Technol. 244 (2014) 131–141, https://doi.org/10.1016/j.surfcoat.2014.01.050.
[4] Z. Pytlicek, M. Bendova, J. Prasek, A. Mozalev, On-chip sensor solution for hydrogen gas detection with the anodic niobium-oxide nanorod arrays, Sens. Actuators, B 284 (2019) 723–735, https://doi.org/10.1016/j.snb.2019.01.009.

[5] Z. Wang, J. Lou, X. Zheng, W.-H. Zhang, Y. Qin, Solution processed Nb_2O_5 electrodes for high efficient ultraviolet light stable planar perovskite solar cells, ACS Sustainable Chem. Eng. 7 (2019) 7421–7429, https://doi.org/10.1021/acssuschemeng.9b00991.

[6] P. Arunkumar, A.G. Ashish, B. Babu, S. Sarang, A. Suresh, C.H. Sharma, M. Thalakulam, M.M. Shaijumon, Nb_2O_5/graphene nanocomposites for electrochemical energy storage, RSC Adv. 5 (2015) 59997–60004, https://doi.org/10.1039/C5RA07895D.

[7] A. Verma, P.K. Singh, Sol-gel derived nanostructured niobium pentoxide thin films for electrochromic applications, Indian J. Chem. 52A (2013) 593–598.

[8] H. García, H. Castán, E. Perez, S. Dueñas, L. Bailón, T. Blanquart, J. Niinistö, K. Kukli, M. Ritala, M. Leskelä, Influence of growth and annealing temperatures on the electrical properties of Nb_2O_5-based MIM capacitors, Semicond. Sci. Technol. 28 (2013), 055005, https://doi.org/10.1088/0268-1242/28/5/055005.

[9] S. Sahoo, Conduction and switching behavior of e-beam deposited polycrystalline Nb_2O_5 based nano-ionic memristor for non-volatile memory applications, J. Alloys Compd. 866 (2021), 158394, https://doi.org/10.1016/j.jallcom.2020.158394.

[10] R. Fiz, L. Appel, A. Gutiérrez-Pardo, J. Ramírez-Rico, S. Mathur, Electrochemical energy storage applications of CVD grown niobium oxide thin films, ACS Appl. Mater. Interfaces 8 (2016) 21423–21430, https://doi.org/10.1021/acsami.6b03945.

[11] N. Li, X. Lan, L. Wang, Y. Jiang, S. Guo, Y. Li, X. Hu, Precisely tunable T-Nb_2O_5 nanotubes via atomic layer deposition for fast-charging lithium-ion batteries, ACS Appl. Mater. Interfaces 13 (2021) 16445–16453, https://doi.org/10.1021/acsami.1c02207.

[12] A. Mozalev, M. Sakairi, I. Saeki, H. Takahashi, Nucleation and growth of the nanostructured anodic oxides on tantalum and niobium under the porous alumina film, Electrochim. Acta 48 (2003) 3155–3170, https://doi.org/10.1016/S0013-4686(03)00345-1.

[13] A. Mozalev, R.M. Vázquez, C. Bittencourt, D. Cossement, F. Gispert-Guirado, E. Llobet, H. Habazaki, Formation–structure–properties of niobium-oxide nanocolumn arrays via self-organized anodization of sputter-deposited aluminum-on-niobium layers, J. Mater. Chem. C 2 (2014) 4847–4860, https://doi.org/10.1039/C4TC00349G.

[14] A. Mozalev, M. Bendova, R.M. Vazquez, Z. Pytlicek, E. Llobet, J. Hubalek, Formation and gas-sensing properties of a porous-alumina-assisted 3-D niobium-oxide nanofilm, Sens. Actuators, B 229 (2016) 587–598, https://doi.org/10.1016/j.snb.2016.02.024.

[15] A. Pligovka, A. Poznyak, M. Norek, Optical properties of porous alumina assisted niobia nanostructured films–Designing 2-D photonic crystals based on hexagonally arranged nanocolumns, Micromachines 12 (22) (2021) 589, https://doi.org/10.3390/mi12060589.

[16] A. Pligovka, A. Lazavenka, G. Gorokh, Anodic niobia column-like 3-D nanostructures for semiconductor devices, IEEE Trans. Nanotechnol. 18 (2019) 790–797, https://doi.org/10.1109/TNANO.2019.2930901.

[17] O. Nishinaga, T. Kikuchi, S. Natsui, R.O. Suzuki, Rapid fabrication of self-ordered porous alumina with 10-/sub-10-nm-scale nanostructures by selenic acid anodizing, Sci. Rep. 3 (2013) 1–6, https://doi.org/10.1038/srep02748.

[18] A.I. Sadykov, S.E. Kushnir, I.V. Roslyakov, A.E. Baranchikov, K.S. Napolskii, Selenic acid anodizing of aluminium for preparation of 1D photonic crystals, Electrochem. Commun. 100 (2019) 104–107, https://doi.org/10.1016/j.elecom.2019.01.027.

[19] M.E. Nasir, S. Peruch, N. Vasilantonakis, W.P. Wardley, W. Dickson, G.A. Wurtz, A. V. Zayats, Tuning the effective plasma frequency of nanorod metamaterials from visible to telecom wavelengths, Appl. Phys. Lett. 107 (2015), 121110, https://doi.org/10.1063/1.4931687.

[20] Y. Shan, Z. Zheng, J. Liu, Y. Yang, L. Zhiyuan, Z. Huang, D. Jiang, Niobium pentoxide: a promising surface-enhanced Raman scattering active semiconductor substrate, npj Comput. Mater. 3 (2017) 11, https://doi.org/10.1038/s41524-017-0008-0.

[21] M. Sepúlveda, K. Kamnev, Z. Pytlicek, J. Prasek, A. Mozalev, Superhydrophobic–oleophobic visible–transparent antireflective nanostructured anodic HfO_2 multifunctional coatings for potential solar panel applications, ACS Appl. Nano Mater. 4 (2021) 1754–1765, https://doi.org/10.1021/acsanm.0c03202.

[22] A.P. Huang, Z.C. Yang, P.K. Chu, Hafnium-based high-k gate dielectrics, in: P. K. Chu (Ed.), Advances in Solid State Circuits Technologies, 2010, pp. 333–350.

[23] S. Tajima, Luminescence, breakdown and colouring of anodic oxide films on aluminium, Electrochim. Acta 22 (1977) 995–1011, https://doi.org/10.1016/0013-4686(77)85011-1.

[24] T. Kikuchi, O. Nishinaga, S. Natsui, R.O. Suzuki, Self-ordering behavior of anodic porous alumina via selenic acid anodizing, Electrochim. Acta 137 (2014) 728–735, https://doi.org/10.1016/j.electacta.2014.06.078.

[25] Y. Nazarkina, K. Kamnev, A. Polokhin, Y. Shaman, The effect of annealing on the Raman spectra of porous anodic alumina films formed in different electrolytes, in: 2017 IEEE Conference of Russian Young Researchers in Electrical and Electronic Engineering, EIConRus), 2017, pp. 1409–1412, https://doi.org/10.1109/EIConRus.2017.7910834.

[26] Y.V. Nazarkina, S.A. Gavrilov, A.A. Polohin, D. Gromov, Y.P. Shaman, Application of porous alumina formed in selenic acid solution for nanostructures investigation via Raman spectroscopy, in: International Conference on Micro-and Nano-Electronics, 2016, pp. 134–138, https://doi.org/10.1117/12.2267148, 10224.

[27] K.C. Bantz, A.F. Meyer, N.J. Wittenberg, H. Im, Ö. Kurtulus, S.H. Lee, N. C. Lindquist, S.-H. Oh, C.L. Haynes, Recent progress in SERS biosensing, Phys. Chem. Chem. Phys. 13 (2011) 11551–11567, https://doi.org/10.1039/C0CP01841D.

[28] M.S. Safavi, F.C. Walsh, L. Visai, J. Khalil-Allafi, Progress in niobium oxide-containing coatings for biomedical applications: a critical review, ACS Omega 7 (2022) 9088–9107, https://doi.org/10.1021/acsomega.2c00440.

[29] H. Cheng, M. Zhang, H. Hu, Z. Gong, Y. Zeng, J. Chen, Z. Zhu, Y. Wan, Selenium-modified TiO_2 nanoarrays with antibacterial and anticancer properties for postoperation therapy applications, ACS Appl. Bio Mater. 1 (2018) 1656–1666, https://doi.org/10.1021/acsabm.8b00486.

[30] N.K. Gupta, A. Fukuoka, K. Nakajima, Amorphous Nb_2O_5 as a selective and reusable catalyst for furfural production from xylose in biphasic water and toluene, ACS Catal. 7 (2017) 2430–2436, https://doi.org/10.1021/acscatal.6b03682.

[31] W. Guan, X. Chen, S. Jin, C. Li, C.-W. Tsang, C. Liang, Highly stable Nb_2O_5–Al_2O_3 composites supported Pt catalysts for hydrodeoxygenation of diphenyl ether, Ind. Eng. Chem. Res. 56 (2017) 14034–14042, https://doi.org/10.1021/acs.iecr.7b03736.

[32] C. Liu, J. Mao, X. Zhang, L. Yu, Selenium-doped Fe_2O_3-catalyzed oxidative scission of CC bond, Catal. Commun. 133 (2020), 105828, https://doi.org/10.1016/j.catcom.2019.105828.

[33] Y.S. Hor, U. Welp, Y. Ito, Z.L. Xiao, U. Patel, J.F. Mitchell, W.K. Kwok, G. W. Crabtree, Superconducting $NbSe_2$ nanowires and nanoribbons converted from $NbSe_3$ nanostructures, Appl. Phys. Lett. 87 (2005), 142506, https://doi.org/10.1063/1.2072847.

[34] A. Mozalev, J. Hubalek, On-substrate porous-anodic-alumina-assisted gold nanostructure arrays: meeting the challenges of various sizes and interfaces, Electrochim. Acta 297 (2019) 988–999, https://doi.org/10.1016/j.electacta.2018.11.192.

[35] V. Surganov, P. Morgen, J.G. Nielsen, G. Gorokh, A. Mozalev, Study of the initial stage of aluminium anodization in malonic acid solution, Electrochim. Acta 32 (1987) 1125–1127, https://doi.org/10.1016/0013-4686(87)90043-0.

[36] Y. Nazarkina, K. Kamnev, A. Dronov, A. Dudin, A. Pavlov, S. Gavrilov, Features of porous anodic alumina growth in galvanostatic regime in selenic acid based electrolyte, Electrochim. Acta 231 (2017) 327–335, https://doi.org/10.1016/j.electacta.2017.02.049.

[37] W. Lee, S.J. Park, Porous anodic aluminum oxide: anodization and templated synthesis of functional nanostructures, Chem. Rev. 114 (2014) 7487–7556, https://doi.org/10.1021/cr500002z.

[38] A. Mozalev, V. Khatko, C. Bittencourt, A.W. Hassel, G. Gorokh, E. Llobet, X. Correig, Nanostructured columnlike tungsten oxide film by anodizing Al/W/Ti layers on Si, Chem. Mater. 20 (2008) 6482–6493, https://doi.org/10.1021/cm801481z.

[39] M. Bendova, J. Kolar, M. Marik, T. Lednicky, A. Mozalev, Influence of nitrogen species on the porous-alumina-assisted growth of TiO_2 nanocolumn arrays, Electrochim. Acta 281 (2018) 796–809, https://doi.org/10.1016/j.electacta.2018.05.197.

[40] A. Mozalev, M. Bendova, F. Gispert-Guirado, E. Llobet, Hafnium-oxide 3-D nanofilms via the anodizing of Al/Hf metal layers, Chem. Mater. 30 (2018) 2694–2708, https://doi.org/10.1021/acs.chemmater.8b00188.

[41] B.R. Strohmeier, An ESCA method for determining the oxide thickness on aluminum alloys, Surf. Interface Anal. 15 (1990) 51–56, https://doi.org/10.1002/sia.740150109.

[42] A.V. Naumkin, V. Kraut-Vass, S.W. Gaarenstroom, C.J. Powell, NIST X-ray Photoelectron Spectroscopy Database. https://srdata.nist.gov/xps/(accessed 18 January 2023).

[43] G.K. Wertheim, F.J. DiSalvo, D.N.E. Buchanan, Site inequivalence in $Fe_{1+x}Nb_{3-x}Se_{10}$, Phys. Rev. B 28 (1983) 3335–3338, https://doi.org/10.1103/PhysRevB.28.3335.

[44] M.C. Biesinger, X-Ray photoelectron spectroscopy (XPS) reference pages, selenium. http://www.xpsfitting.com/search/label/Selenium. (Accessed 18 January 2023).

[45] G.E. Thompson, G.C. Wood, Porous anodic film formation on aluminium, Nature 290 (1981) 230–232, https://doi.org/10.1038/290230a0.

[46] I. Vrublevsky, V. Parkoun, V. Sokol, J. Schreckenbach, Analysis of chemical dissolution of the barrier layer of porous oxide on aluminum thin films using a re-anodizing technique, Appl. Surf. Sci. 252 (2005) 227–233, https://doi.org/10.1016/j.apsusc.2005.02.024.

[47] M. Bendova, Z. Pytlicek, J. Prasek, A. Mozalev, The growth and unique electronic properties of the porous-alumina-assisted hafnium-oxide nanostructured films, Electrochim. Acta 327 (12) (2019), 135029, https://doi.org/10.1016/j.electacta.2019.135029.

[48] A. Mozalev, Z. Pytlicek, K. Kamnev, J. Prasek, F. Gispert-Guirado, E. Llobet, Zirconium oxide nanoarrays via the self-organized anodizing of Al/Zr bilayers on substrates, Mater. Chem. Front. 5 (2021) 1917–1931, https://doi.org/10.1039/D0QM00862A.

[49] M. Bendova, J. Hubalek, A. Mozalev, Exploring electron transport and memristive switching in nanoscale Au/WO_x/W multijunctions based on anodically oxidized Al/W metal layers, Adv. Mater. Interfac. 3 (12) (2016), 1600512, https://doi.org/10.1002/admi.201600512.

[50] M. Bendova, F. Gispert-Guirado, A.W. Hassel, E. Llobet, A. Mozalev, Solar water splitting on porous-alumina-assisted TiO_2-doped WO_x nanorod photoanodes: paradoxes and challenges, Nano Energy 33 (2017) 72–87, https://doi.org/10.1016/j.nanoen.2017.01.029.

[51] Y. Kim, K. Yuan, B.R. Ellis, U. Becker, Redox reactions of selenium as catalyzed by magnetite: lessons learned from using electrochemistry and spectroscopic methods, Geochem. Cosmochim. Acta 19 (2017) 304–323, https://doi.org/10.1016/j.gca.2016.10.039.

[52] W.M. Haynes, CRC Handbook of Chemistry and Physics, CRC press, 2016.

[53] K. Baek, N. Kasem, A. Ciblak, D. Vesper, I. Padilla, A.N. Alshawabkeh, Electrochemical removal of selenate from aqueous solutions, Chem. Eng. J. 215 (2013) 678–684, 10.1016%2Fj.cej.2012.09.135.
[54] A.J. Bard, L.R. Faulkner, Electrochemical Methods: Fundamentals and Applications, John Wiley & Sons, Inc., 2001.
[55] X. Tan, J. Melkersson, S. Wu, L. Wang, J. Zhang, Noble–metal–free materials for surface–enhanced Raman spectroscopy detection, ChemPhysChem 17 (2016) 2630–2639, https://doi.org/10.1002/cphc.201600286.
[56] L. Yang, Y. Wei, Y. Song, Y. Peng, Y. Yang, Z. Huang, Surface-enhanced Raman scattering from amorphous nanoflower-structural Nb_2O_5 fabricated by two-step hydrothermal technology, Mater. Des. 193 (2020), 108808, https://doi.org/10.1016/j.matdes.2020.108808.
[57] T. Gao, G. Meng, L. Zhang, Blue luminescence in porous anodic alumina films: the role of the oxalic impurities, J. Phys. Condens. Matter 15 (2003) 2071–2079, https://doi.org/10.1088/0953-8984/15/12/324.
[58] I. Vrublevsky, K. Chernyakova, A. Ispas, A. Bund, N. Gaponik, A. Dubavik, Photoluminescence properties of heat-treated porous alumina films formed in oxalic acid, J. Lumin. 131 (2011) 938–942, https://doi.org/10.1016/j.jlumin.2010.12.027.
[59] L. Mitterhuber, E. Kraker, S. Defregger, Structure function analysis of temperature-dependent thermal properties of nm-thin Nb_2O_5, Energies 12 (14) (2019) 610, https://doi.org/10.3390/en12040610.
[60] J.M. Jehng, I.E. Wachs, Structural chemistry and Raman spectra of niobium oxides, Chem. Mater. 3 (1991) 100–107, https://doi.org/10.1021/cm00013a025.
[61] N. Li, G. Xu, M. Yan, B. Chen, Y. Yuan, C. Zhu, Fabrication of vertically aligned ZnO nanorods modified with dense silver nanoparticles as effective SERS substrates, Chemosensors 11 (2023) 210, https://doi.org/10.3390/chemosensors11040210.
[62] L.N. Liu, H.W. Choi, J.P. Xu, P.T. Lai, High-performance GaAs metal-oxide-semiconductor capacitor by using NbAlON as high-k gate dielectric, Appl. Phys. Lett. 110 (2017), 123506, https://doi.org/10.1063/1.4979101.
[63] K. Kamnev, M. Sepúlveda, M. Bendova, Z. Pytlicek, J. Prasek, E. Kolibalova, J. Michalicka, A. Mozalev, The growth, composition, and functional properties of self-organized nanostructured ZrO_2-Al_2O_3 anodic films for advanced dielectric applications, Adv. Electron. Mater. 7 (2021), 2100505, https://doi.org/10.1002/aelm.202100505.
[64] A. Mozalev, M. Sakairi, H. Takahashi, H. Habazaki, J. Hubálek, Nanostructured anodic-alumina-based dielectrics for high-frequency integral capacitors, Thin Solid Films 550 (2014) 486–494, https://doi.org/10.1016/j.tsf.2012.02.077.
[65] K. Kamnev, Z. Pytlicek, M. Bendova, J. Prasek, F. Gispert-Guirado, E. Llobet, A. Mozalev, The planar anodic Al_2O_3-ZrO_2 nanocomposite capacitor dielectrics for advanced passive device integration, Sci. Technol. Adv. Mater. 24 (2023), 2162324, https://doi.org/10.1080/14686996.2022.2162324.
[66] J. Azadmanjiri, C.C. Berndt, J. Wang, A. Kapoor, V.K. Srivastava, C. Wen, A review on hybrid nanolaminate materials synthesized by deposition techniques for energy storage applications, J. Mater. Chem. A 2 (2014) 3695–3708, https://doi.org/10.1039/C3TA14034B.
[67] S. Clima, G. Pourtois, S. Van Elshocht, S. De Gendt, M.M. Heyns, D.J. Wouters, J. A. Kittl, Dielectric response of Ta_2O_5, $NbTaO_5$ and Nb_2O_5 from first-principles investigations, ECS Trans. 19 (2009) 729–737, https://doi.org/10.1149/1.3122128.
[68] E.O. Filatova, A.S. Konashuk, Interpretation of the changing the band gap of Al_2O_3 depending on its crystalline form: connection with different local symmetries, J. Phys. Chem. C 119 (2015) 20755–20761, https://doi.org/10.1021/acs.jpcc.5b06843.
[69] D. Martin, M. Grube, W. Weinreich, J. Müller, W.M. Weber, U. Schröder, H. Riechert, T. Mikolajick, Mesoscopic analysis of leakage current suppression in $ZrO_2/Al_2O_3/ZrO_2$ nano-laminates, J. Appl. Phys. 113 (2013), 194103, https://doi.org/10.1063/1.4804670.
[70] M.B. Zakaria, T. Nagata, T. Chikyow, Mesostructured HfO_2/Al_2O_3 composite thin films with reduced leakage current for ion-conducting devices, ACS Omega 4 (2019) 14680–14687, https://doi.org/10.1021/acsomega.9b01095.
[71] A.B.D. Cassie, S. Baxter, Wettability of porous surfaces, Trans. Faraday Soc. 40 (1944) 546–551, https://doi.org/10.1039/TF9444000546.
[72] B. Reichman, A.J. Bard, Electrochromism at niobium pentoxide electrodes in aqueous and acetonitrile solutions, J. Electrochem. Soc. 127 (1980) 241–242, https://doi.org/10.1149/1.2129628.
[73] J. Xia, N. Masaki, K. Jiang, S. Yanagida, Fabrication and characterization of thin Nb_2O_5 blocking layers for ionic liquid-based dye-sensitized solar cells, J. Photochem. Photobiol., A 188 (2007) 120–127, https://doi.org/10.1016/j.jphotochem.2006.11.028.
[74] Z. Fohlerova, K. Kamnev, M. Sepúlveda, Z. Pytlicek, J. Prasek, A. Mozalev, Nanostructured zirconium-oxide bioceramic coatings derived from the anodized Al/Zr metal layers, Adv. Mater. Interfac. 8 (2021), 2100256, https://doi.org/10.1002/admi.202100256.
[75] Z. Fohlerova, A. Mozalev, Anodic formation and biomedical properties of hafnium-oxide nanofilms, J. Mater. Chem. B 7 (2019) 2300–2310, https://doi.org/10.1039/C8TB03180K.
[76] Z. Fohlerova, A. Mozalev, Tuning the response of osteoblast–like cells to the porous–alumina–assisted mixed–oxide nano–mound arrays, J. Biomed. Mater. Res. B Appl. Biomater. 106 (2018) 1645–1654, https://doi.org/10.1002/jbm.b.33971.
[77] P. Whanger, S. Vendeland, Y.C. Park, Y. Xia, Metabolism of subtoxic levels of selenium in animals and humans, Ann. Clin. Lab. Sci. 26 (1996) 99–113.
[78] X. Chen, K. Cai, J. Fang, M. Lai, Y. Hou, J. Li, Z. Luo, Y. Hu, L. Tang, Fabrication of selenium-deposited and chitosan-coated titania nanotubes with anticancer and antibacterial properties, Colloids Surf., B 103 (2013) 149–157, https://doi.org/10.1016/j.colsurfb.2012.10.022.
[79] P. Bernard, P. Stelmachowski, P. Broś, W. Makowski, A. Kotarba, Demonstration of the influence of specific surface area on reaction rate in heterogeneous catalysis, J. Chem. Educ. 98 (2021) 935–940, https://doi.org/10.1021/acs.jchemed.0c01101.
[80] F.V. Singh, T. Wirth, Selenium reagents as catalysts, Catal. Sci. Technol. 9 (2019) 1073–1091, https://doi.org/10.1039/C8CY02274G.